EFFECTS OF ULTRATHIN INTERLAYERS ON THERMAL BOUNDARY CONDUCTANCE AT METAL-DIELECTRIC INTERFACES

SHANY MARY OOMMEN

A THESIS SUBMITTED TO
THE FACULTY OF GRADUATE STUDIES
IN PARTIAL FULFILLMENT OF THE REQUIREMENTS
FOR THE DEGREE OF
MASTER OF SCIENCE

GRADUATE PROGRAM IN PHYSICS AND ASTRONOMY
YORK UNIVERSITY
TORONTO, ONTARIO

May 2019

ABSTRACT

Heat transport in micro- and nano-scale materials have an increasingly important role in thermal management of numerous technologies such as thermoelectric energy conversion, microelectronics, and plasmonic devices. Understanding the heat transport contributions from the interface is crucial when interfacial resistance forms a significant fraction of the total thermal resistance of the device.

In this thesis, we analyze the modification of thermal conductance at metal-dielectric interfaces by inserting few-nanometer thick metal interlayers. A thickness-dependent interlayer study suggests that interfacial conductance alters significantly at ultrathin thicknesses before reaching a plateau. Our results reveal that the electron-phonon coupling strength of an interlayer plays a significant role in determining the overall thermal boundary conductance. Analysing heat transport mechanisms across a variety of metal-dielectric interfaces by means of an interlayer indicated that thermal boundary conductance depends on an interplay between the phonon vibrational properties and metal electron-phonon coupling strength overlap.

ACKNOWLEDGMENTS

First and foremost, I express my sincere gratitude to my supervisor, Dr. Simone Pisana, for his invaluable guidance, motivation, and support. I have learned many valuable skills and much knowledge under his structured and diligent guidance. I appreciate him for contributing his ideas, support, critiques, and time to successfully complete this work. I would like to thank the members of the supervisory committee for their time and for agreeing to be a part of this thesis.

I am immensely grateful to the members of The Heated Lab for their generous advice and support. I owe special thanks to Olga Andriyevska and Mohammadreza Shahzadeh for their wonderful friendship and constant encouragement during tough times.

I would also like to thank our collaborator, Hellwig group in Technische Universität Chemnitz and Helmholtz-Zentrum Dresden-Rossendorf, for providing samples for thermal transport measurements.

Finally, I want to thank my family and friends for making my life lively and fun.

TABLE OF CONTENTS

LIST OF TABLES

LIST OF FIGURES

LIST OF ACRONYMS

HAMR	Heat Assisted Magnetic Recording
DOS	Density of States
AMM	Acoustic Mismatch Model
DMM	Diffuse Mismatch Model
BZ	Brillouin Zone
TDTR	Time Domain Thermoreflectance
EOM	Electro-Optic Modulator
TTM	Two-Temperature Model

CHAPTER 1

INTRODUCTION

Engineering nanomaterials and exploiting their thermal, electrical, optical, and mechanical properties have led to momentous advancements in the field of science and technology [1]–[4]. The various thermo-physical properties associated with the nanomaterials are significantly different from their bulk counterpart due to scattering of energy carriers, band structure modifications, and modification of scattering phase space. Enhancement of surface-to-volume ratio in nanostructures alters the energy carrier scattering pathways due to their spatial confinement. The carrier confinement in nanomaterials can modify their velocity, dispersion, and density of states [5]. Interfaces play an important role in nanoscale heat transport. In contrast to bulk, interfaces in nanoscale materials offer new resistance channels for heat carriers to travel, and detailed knowledge of heat transport at the interface is required in numerous significant technologies [1]–[3], [6]. For example, highly efficient thermoelectric devices require a high figure of merit, $ZT = S\sigma^2 T/k$, where S is the Seebeck coefficient, σ is the electrical conductivity, T is the temperature, and $k=k_e+k_p$ is the total thermal conductivity due to phonons (k_p) and electrons (k_e). ZT can be improved either by enhancing the thermoelectric power factor ($S\sigma^2$) or by reducing the thermal conductivity k [7], [8], [9]. Since σ and k_e are interrelated, reducing the phonon thermal conductivity of the thermoelectric material is the most preferred way for enhancing the thermoelectric efficiency [10], [11]. Another obvious example is the heat generation in heat-assisted magnetic recording (HAMR) devices [12]. Here, a metallic near field transducer (NFT) heats a magnetic medium by concentrating laser energy to a spot. To avoid self-heating, the heat

generated in the NFT metal due to plasmonic heating must dissipate to a nearby dielectric through a boundary. This has to be achieved while preserving the low-loss character of the optical device. Heat dissipation at the metal-dielectric interface can be maximized by properly modifying the interfacial thermal properties. Interfacial thermal transport can be expressed using thermal boundary conductance (G) defined by:

$$G = {}^{q}/_{\Delta T} \quad (1)$$

Here, q is the heat flux across the boundary and ΔT is the temperature difference. G can be modified (enhanced or reduced) by tuning the various factors affecting interfacial heat transport. The details of the various factors that affect thermal boundary conductance are explained in Section 1.1.3.

In this study, we strive to understand and tune the interfacial thermal conductance, particularly the conductance at the metal-dielectric interface. One possible approach to modify the interfacial boundary conductance of such a system is to insert an appropriate interlayer between the metal and dielectric [13], [14]. This project involves utilizing an ultrafast pump-probe set-up to investigate the thermal transport at the metal-dielectric interface with sub-nanometer adhesion layers.

1.1 Background

1.1.1 Nanoscale heat transport

Thermal energy in materials propagates due to random motion of heat carriers. Macroscopically, heat transfer occurs in three different modes: conduction, convection, and

thermal radiation. The heat transfer process is accomplished by microscopic collisions of energy carriers (e.g.: charge carriers, atoms, molecules, nuclei, etc.) until the system reaches thermal equilibrium. The thermal conductivity (k) is defined as the ability of a material to transfer thermal energy from high-temperature to low-temperature regions. Thermal conductivity is an intensive property (independent of size and geometry) for bulk materials. Classical heat transfer processes can be analyzed based on Fourier's law. Fourier's law of heat conduction states that heat flux across a material with thermal conductivity k is directly proportional to the temperature gradient along the direction of heat flux as [2]:

$$J = -k\frac{dT}{dx} \tag{2}$$

where dT/dx is the temperature gradient across the material.

When the material size shrinks from bulk to micro- or nano-scales, the heat transport mechanism changes, and size constraints significantly alter thermal properties. As a result, heat transport in materials deviates significantly from Fourier's law predictions. Thermal conductivity of the nanomaterials can become thickness dependent and anisotropic [15]. The validity of Fourier's law will be discussed later in this section. Microscopically, the total thermal conductivity of a material is the summation of thermal conductivities due to individual heat carriers. The quantitative energy associated with each energy carriers can be determined from quantum mechanical principles [2], [16].

Phonons or lattice vibrations are the major heat carriers in dielectrics and semiconductors. Phonons are quantized lattice vibrations, which follow Bose-Einstein statistics. Dispersion relation $\omega(q)$ for phonons gives allowable energy (or frequency (ω)) values as a function of wavevector q. For any three-dimensional lattice (three degrees of freedom), the total number of phonon modes is

given by 3*N*, where *N* corresponds to the number of atoms per primitive cell [16]. Phonons can be of two types: acoustic (propagates at the speed of sound) and optical (interacts with an external electromagnetic field) phonons. Acoustic phonons are low-frequency lattice vibrations caused by in-phase displacement of neighboring atoms in a solid. In a longitudinal acoustic mode, atoms are displaced parallel to the direction of wave propagation, whereas in transverse mode atoms are displaced perpendicular to the wave propagation direction. In the long wavelength regime, acoustic phonons converge to zero at the Brillouin zone (BZ) center (see Fig. 1.1), and the dispersion relation exhibits a linear trend [16]. In contrast, optical phonons are caused by opposite displacements of neighboring atoms in a lattice, and are, therefore, high in energy. Opposite

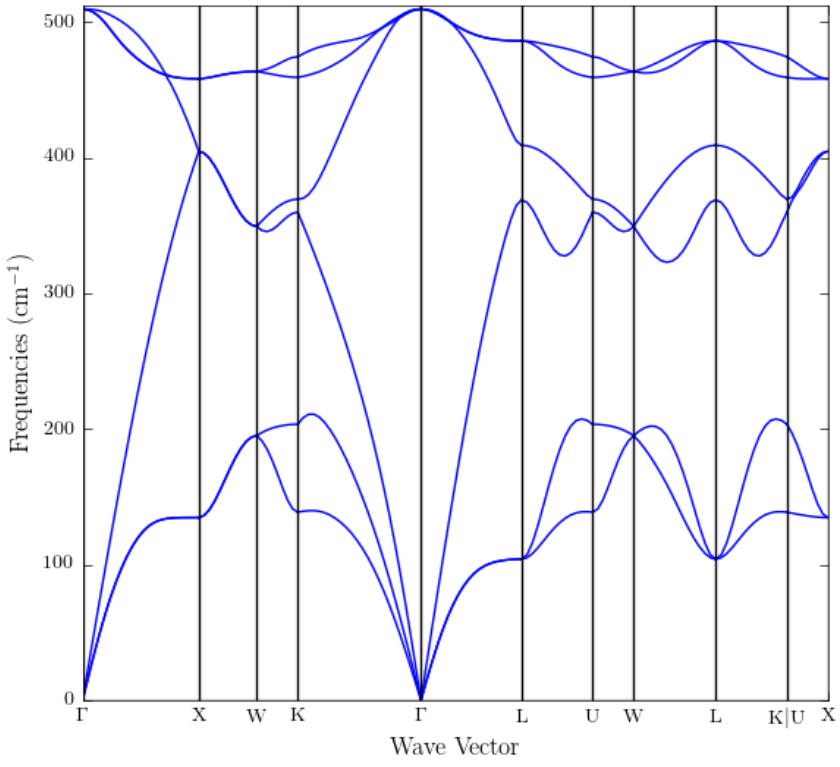

Fig. 1.1. Phonon dispersions in Si along different crystallographic directions [17].

displacements require multiple atoms (e.g. sapphire, quartz) in the lattice unit cell. At the zone center, frequency of optical phonons are non-zero. For any real lattice, the total number of acoustic and optical phonons are given by three and 3*N*-3, respectively.

For example, in a monoatomic lattice (one atom per primitive cell, e.g. Al, Cr), there are a total of three phonon branches, whereas in a diatomic solid (e.g. diamond, magnesium), there are a total of six phonon modes, with three acoustic and three optical branches. Phonon dispersions are different along different crystallographic directions. Fig. 1.1 shows the phonon dispersion in Si [17]. Si has a diatomic lattice, and so it has six phonon branches.

Free electrons (conduction band electrons) primarily govern thermal transport in metals. Electrons obey Fermi-Dirac distribution. Similar to phonon band structure, electron dispersion relation gives the relation between electron energy and wavevector. Free electrons travel at a high velocity (~10^6 m/s) inside the metal until they get scattered by phonons, electrons or impurities.

Heat transfer results from random motion of energy carriers. Scattering mechanisms involving energy carriers can be characterized by relaxation time, τ. Relaxation time can be defined as the average time taken by energy carriers between successive collisions. Phonons traveling across a material can be scattered in many ways. Matthiessen's rule calculates the overall relaxation time (τ_T) for phonons and is given by:

$$\frac{1}{\tau_T} = \frac{1}{\tau_{p-p}} + \frac{1}{\tau_I} + \frac{1}{\tau_B} + \frac{1}{\tau_{p-e}} \qquad (3)$$

where $\tau_{p-p}, \tau_I,\ \tau_B, \tau_{p-e}$ are relaxation time for phonon-phonon scattering, phonon-impurity scattering, phonon-boundary scattering, and phonon-electron scattering, respectively [2]. For electrons in a metal, the dominant scattering process is electron-phonon scattering. In the presence

of more scattering sources (such as impurities), Matthiessen's rule for electrons can be used to analyze their combined effects.

Thermal properties deviation from bulk can happen due to size constraints in nanomaterials, which imposes additional boundary condition. Size effect appears when the material size is comparable to or smaller than the mean free path of energy carriers [18]. Mean free path (Λ) can be defined as the average distance traveled by the energy carriers between successive collisions. The typical mean free paths for electrons and phonon range between ~1 nm-1 μm. The thermal conductivity of nanomaterials can significantly change from bulk at these length scales due to frequent collisions with the boundaries which are absent in bulk [19], [20]. Spatial confinement of phonons in nanomaterials can alter their band structure, which in turn modifies the phonon properties. Therefore, size effects can modify thermal transport properties in nanomaterials compared to their bulk counterparts. When the mean free path of energy carrier is much smaller than material size, and with a sufficient number of scatterings to achieve equilibrium, transport is described as '*diffusive'*. When the mean free path is much larger than material size with no or few scatterings events, transport is '*ballistic'*. The intermediate regime between the above-mentioned transport processes is called '*semi-ballistic'*. Fourier's law is only valid for diffusive transport because it fails to capture ballistic and semi-ballistic effects. In addition to this, Fourier's law is also invalid for heat transport processes faster than the relaxation time of energy carriers (typically ranging between ~10^{-12}-10^{-10} s) [2]. This is because classical Fourier's law was developed assuming multiple random collisions of energy carriers, and the law deviates when collisions are absent.

1.1.2 Heat transport pathways in metal-dielectric system after ultrafast laser heating

Heating and subsequent thermal processes after the absorption of an ultrafast pulse laser involve many sequential pathways (different from steady state heating). For a metal-dielectric system, the laser pulse incident on the sample surface is initially absorbed by the free electrons in the metal, rapidly raising the electron temperature in a few femtoseconds. Subsequently, the electrons undergo numerous scattering mechanisms with each other (10-100 fs) and with the lattice to transfer the energy (0.1-10 ps). Electron-lattice energy transfer process happens at a time scale similar to the relaxation time of electrons and phonons. Both electron and phonon population reaches a thermal equilibrium in a few picoseconds (~1-100 ps in metals), depending on the electron-phonon coupling constant (g), electronic heat capacity, (C_e) and phonon heat capacity (C_p). Eventually, within few nanoseconds, heat dissipates to the dielectric substrate across a boundary.

In a metal-dielectric system, heat conduction is primarily governed by scattering mechanisms involving electrons and phonons. At the boundary, there exist different pathways to transfer the energy from the metals to the dielectric (Fig. 1.2). There are two major pathways. In *pathway 1*, electrons in the metal couple with the phonons in the metal. Subsequently, these phonons transfer energy to the phonons in the dielectric. In *pathway 2*, a direct coupling exists between electrons in the metal and phonons in the dielectric at the interface. The interfacial resistance in *pathway 1 (R_1)* and *pathway 2 (R_2)* can be calculated as:

$$R_1 = R_{ep} + R_{pp} \quad (4)$$

$$R_2 = R_{ep,i} \quad (5)$$

where, R_{ep} is the resistance due to electron-phonon coupling within the metal, R_{pp} is the resistance due to phonon-phonon interaction between the metal and dielectric substrate, and $R_{ep,i}$ is the resistance due to the direct electron-phonon coupling between the metal and dielectric. The total interfacial resistance of the metal-dielectric system can be expressed assuming the resistance due to two pathways are parallel to each other as:

$$R_T = \frac{R_1 R_2}{R_1 + R_2} \tag{6}$$

Numerous studies have been conducted to explore both pathways [21]–[27]. Majumdar and Reddy [21] studied the contribution of electron-phonon coupling at a metal-dielectric interface using the two-temperature model for electrons and phonons. They suggested that the conductance due to electron-phonon coupling can be expressed as $\sqrt{gk_p}$, where g is the volumetric electron-phonon coupling constant, and k_p is the thermal conductivity of phonons in metal. R_{pp} at the interface can be evaluated assuming an acoustic mismatch model (AMM) or diffuse mismatch model (DMM) [28]. AMM assumes a flat interface and phonon transmission is due to the difference in acoustic impedance of the two materials. DMM is based on the assumption that a rough interface destroys acoustic correlations between incident and transmitted phonons. Further details of the models are explained in Chapter 3. There have been several attempts to study the effect of interfacial electron-phonon coupling [23], [25], [26]. For example, Giri et al. showed that electron-phonon scattering at the interface contributes to the interfacial thermal conductance only when electron temperature is much higher than the phonon temperature [25]. Note that for technological applications, the typical electron temperatures are relatively lower, hence the contribution from $R_{ep,i}$ is not so important. Hopkins and Norris [26] suggested that at very high electron-phonon non-equilibrium, direct coupling between electrons in metal and phonons in

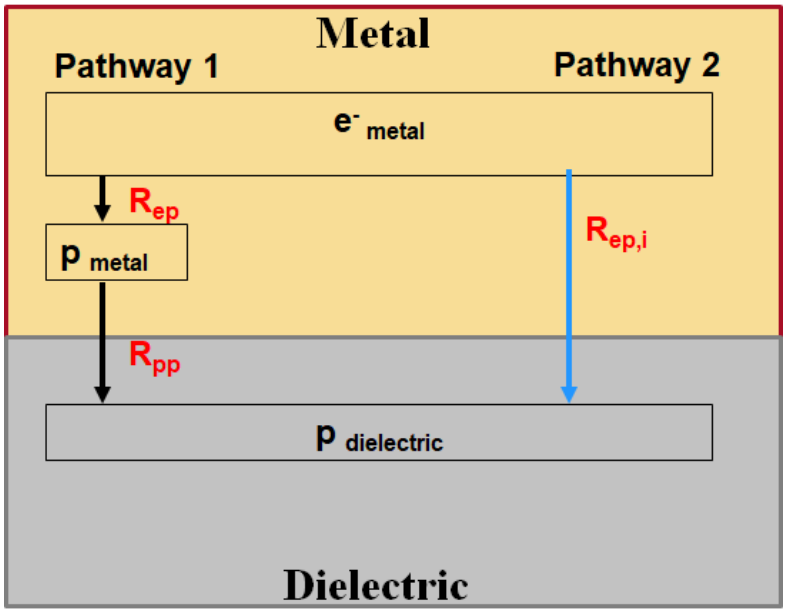

Fig. 1.2. Heat transfer pathways at metal-dielectric interface. *Pathway 1* and *pathway 2* represent two heat transfer pathways between electrons in metal (e^-_{metal}) and phonons in dielectric ($P_{dielectric}$). Black solid arrow and blue solid arrow represents the direction of heat transport in *pathway 1* and *pathway 2*, respectively.

substrate plays a significant role in determining *G* and can be predicted using a three-temperature model. They showed that increasing the laser fluence from 1 Jm^{-2} to 15 Jm^{-2} can increase the electron temperature resulting in enhanced electron-phonon non-equilibrium. Our experiments were done at a low laser fluence of ~2 Jm^{-2}. Hence, in our analysis, we ignore the contribution from the resistance due to interfacial electron-phonon coupling.

1.1.3 Factors affecting interfacial thermal transport in metal-dielectric system

In micro- and nano-scale systems, interfaces significantly affect heat transport due to an abrupt temperature drop across the interface. As mentioned earlier, interfacial thermal transport

dominates total heat transport in nanosystems due to its large contribution to the overall thermal resistance of the material. Interfacial heat transport mechanisms provide additional ways to tune the heat transport which is critical in heat management applications [8], [11], [12], [29]. Understanding the contributions from interfacial transport is more important in fabricating and engineering novel micro and nano-electronic devices. For example, increasing efficiency of thermoelectric materials by using nanostructured materials with reduced thermal conductivity is a well-adapted approach in thermoelectric energy conversions. This can be achieved either by enhancing phonon scattering mechanisms or by modifying the dispersion relations via phonon confinement in nanowires, superlattices, and other low-dimensional systems [5], [8], [11], [20], [29]. The first process requires a thorough understating of interfacial properties.

Thermal transport at a metal-dielectric interface depends on several factors, such as interface quality (interface roughness, grain boundaries, interfacial defects, and interfacial bonding), electron-phonon coupling strength, and interfacial phonon mismatch. There have been extensive studies done to understand various properties and their effects on interfacial thermal transport, but tuning or modifying the interfacial conductance remains a major challenge. For example, Duda and Hopkins [30] demonstrated that the interfacial boundary conductance can be reduced by introducing *roughness* at the interface. They introduced roughness at Al/Si interface by depositing Al thin films on chemically etched Si substrates. They showed that increasing roughness substantially reduces thermal boundary conductance due to increased phonon scattering at the interface. Another factor that significantly affects the thermal boundary conductance is *interfacial bonding* [31], [32]. Ref [31] suggests that chemical functionalization of single-layer graphene (SLG) with oxygen enhances thermal boundary conductance between Al/SLG/SiO_2

layers. This is due to enhanced covalent bonding density in Al/O-SLG/SiO_2. Better interfacial bonding provides a stronger bond, thereby increasing the phonon transmission across the interface.

Modifying the interfacial properties by the addition of a metallic interlayer is an area of active research [13], [14], [33], [34]. Wang et al. [33], using Boltzmann transport simulations suggested that the insertion of an interlayer with intermediate *electron-phonon coupling strength* at a metal-dielectric interface significantly enhances interfacial thermal boundary conductance. They studied the effect of Al and Pt interlayer at Au/Si interface with interlayer thickness varied between 10 nm to 100 nm. Au has a lower g among other common metals at room temperature (For Au, g= 0.023×10^{18} W/m^3K). This introduces a strong electron-phonon non-equilibrium in Au layer, enhancing resistance R_{ep} $\left(R_{ep} = 1/\sqrt{gk_p}\right)$. This process, in turn, reduces the overall G at Au-Si interface (Eq. 4). Interlayers with electron-phonon coupling strength higher than Au enhance the boundary conductance by readily dragging non-equilibrated electrons and phonons into equilibrium. Ref. [35] showed that insertion of a 20 nm thick Ni interlayer at Au/Sapphire interface can reduce the interfacial resistance by 70% due to the strong electron-phonon coupling in Ni. An enhancement in thermal boundary conductance on addition of a 3 nm Ti interlayer at Au/Al_2O_3 and Au/SiO_2 boundaries was demonstrated by ref. [35]. They attributed boundary conductance enhancement to strong electron-phonon coupling constant of the Ti interlayer. Moreover, they suggested that the Ti interlayer enhances interfacial bonding with the substrate and thus improves interfacial conductance.

Using non-equilibrium molecular dynamics simulations, English et al. show that thermal boundary conductance at any solid-solid interface can be tuned by adding an interlayer with intermediate *vibrational spectra* [34]. Cheaito et al. studied both experimentally and theoretically the thermal boundary conductance accumulation function across a range of metal/native oxide/Si

and metal/sapphire systems [36]. The study provided better understanding of phonon interactions with interface to transfer energy and their spectral contribution to *G*. A better overlap between metal and dielectric phonon dispersions can enhance *G* either due to the change in phonon energy flux at the interface or due to the change in phonon transmission across the interface (Eq. 27 and 28). Accumulation function can be calculated by taking a product of weighted average of interfacial phonon transmission function and accumulation of temperature derivative of phonon flux incident on the interface [36]. They showed that experimentally accumulation function can be calculated by varying metals with different *cut-off frequencies* (maximum-frequency) on the same substrate. Because, this provides a way to change the phonon flux in a metal, which determines the accessible phonons in the dielectric, which in turn can couple with phonons in metal. They showed that increasing metal-cut-off frequencies enhances *G* by increasing the phonon flux at the interface. They also reported that heat transport across the interface depends on the relative position of metal and substrate cut-off frequencies rather than Debye temperature. This is due to the fact that the *G* for Al/sapphire system is greater than the *G* for Al/Si system, in spite of it having a relatively low Debye frequency mismatch between metal and substrate as compared to Al/sapphire. The observation can be better explained in terms of phonon cut-off frequencies since Al/sapphire cut-off frequencies overlap better than Al/Si.

Jeong et al. [13] conducted experimental and theoretical thickness-dependence studies for metallic interlayers below 10 nm. They reported that the insertion of a metal layer between a metal and dielectric with an intermediate *Debye temperature* could significantly increase the thermal boundary conductance. The authors showed that inserting Cr and Cu interlayers at Au/sapphire interface enhances the thermal boundary conductance by ~80% and ~60%, respectively. Theoretical modeling of thermal boundary conductance was done using a modified diffuse

mismatch model assuming that phonons with wavelength larger than interlayer thickness transfers directly from Au layer and the phonons with wavelength smaller than interlayer thickness come from the interlayer. Thus, the interlayer contributes to the overall thermal boundary conductance only when the phonon wavelength is smaller than the interlayer thickness. However, they neglected all other factors that can contribute to the thermal boundary conductance. Blank and Weber [14] demonstrated the effect of Cu interlayer with thickness ranging between 1.5 nm-30 nm at Au/Sapphire, Au/Si, and Au/diamond interfaces. They suggested that the contribution of electron-phonon coupling in the interlayer should be taken into account while analyzing the data.

The above-mentioned studies pointed out the various factors such as Debye temperature, phonon cut-off frequency, electron-phonon coupling in interlayer, and interfacial electron-phonon coupling that can affect the heat transport in the presence of an interlayer. As mentioned earlier, Ref. [13], [14] carried out an experimental thickness-dependent analysis of thermal boundary conductance with ultrathin interlayers. However, so far, no studies have been done to systematically analyze the various heat transfer pathways that contribute to thermal boundary conductance on addition of an interlayer. Systematic analysis of various factors that affect the heat transfer pathways is required to properly tune (enhance/reduce) the thermal boundary conductance at a metal-dielectric interface. This thesis tries to address the following problems:

1) How does *G* vary with interlayer thickness?
2) Which heat transfer pathways are dominant in the presence of a particular interlayer?
3) What interlayer properties enhances/reduces the *G*?
4) How to select an interlayer to enhance/reduce *G*?

To answer these questions, we did an experimental and theoretical analysis of a series of metal-dielectric interfaces by inserting various interlayers. As shown in Fig. 1.1, thermal transport from metal to dielectric is primarily controlled by phonon-metal/phonon-dielectric interaction. Hence, one way to tune the metal-dielectric interfacial transport is by tuning the phonon interaction. Phonon interaction at a metal-dielectric interface can be enhanced by adding an interlayer with intermediate vibrational properties; this is due to the better overlap between vibrational spectra of metal and dielectric. The vibrational overlaps can be conveniently expressed in terms of phonon density of states overlap, which determines the available number of phonon states in a small wavevector interval $q+dq$. or overlap between phonon acoustic cut-off frequency, which can be determined from real phonon dispersion relations (no approximation in dispersion relations). Assuming a linear Debye approximation ($\omega=cq$), phonon density of states is given by:

$$D(\omega) = \frac{3\omega^2}{2v^3\pi^2} \quad (7)$$

Here, ω is the phonon frequency and v is the speed of sound. This is valid up to ω_c, which is the Debye cut-off frequency [37]. ω_c is directly proportional to the Debye temperature ($\omega_c = \hbar\theta_D/K_B$ where, $\hbar$ is the reduced Planck's constant and K_B is the Boltzmann constant). Thus, under the linear approximation, Debye temperature is a direct measure of phonon density of states. Ref. [13] shows that inserting interlayers with intermediate θ_D enhances the overall thermal boundary conductance at a metal-dielectric interface. Interlayers with higher θ_D than top metal layer have more available phonon states, and hence can have a better overlap with dielectric substrate with even higher θ_D. Thus, availability of more phonon modes enhances the phonon flux at the interface, which results in an enhancement in the overall G.

On the other hand, the phonon cut-off frequencies from real phonon dispersion branch gives the maximum phonon frequency in a particular material. Materials with high phonon

frequency have high phonon density of states (in essence, have more available phonon states), which in turn enhances the phonon flux at the interface. Alternatively, materials with high cut-off frequencies have more high-energy phonons, which increases the energy flux at the interface. The phonon flux through an interface due to a specific phonon mode is directly proportional to temperature gradient across the interface, the group velocity and the number density of the phonon mode. Hence, cut-off frequency is a good measure of phonon flux at the interface. Inserting an interlayer with intermediate phonon cut-off frequency at a metal-dielectric interface can enhance the *G* due to the enhancement in phonon flux at the interface.

Another significant factor that affects the heat transport at metal-dielectric interface is the electron-phonon coupling strength, *g*. As explained previously, interlayers with *g* higher than top metal layer reduce the electron-phonon non-equilibrium by immediately dragging them into thermal equilibrium. This process enhances the overall thermal boundary conductance, as it facilitates the process of energy transfer between the electrons in the metal to the phonons in the dielectric [33]. The effects of non-equilibrium are more pronounced when the top metal layer has a very small *g*, which increases the equilibrium time between phonons and electrons. In addition to this, previous studies showed that additional heat transfer pathways can be created depending on the strength of interlayer electron-phonon coupling [25].

Thus, the modification of thermal boundary conductance requires the proper understanding of the above-mentioned factors such as Debye temperature, phonon cut-off frequency, and electron-phonon coupling. In order to understand these factors, we analyze a series of metal-dielectric interfaces in the presence of various interlayers. Interlayers were selected based on the assumption that adding an interlayer with intermediate vibrational properties and electron-phonon

coupling constant should enhance the overall thermal boundary conductance. Further details on choices made on interlayers can be found in Chapter 4 and Chapter 5.

1.2 Thesis scope and outline

This thesis is concerned with theoretical and experimental analysis of the influence of ultrathin metallic interlayers on interfacial thermal transport at metal-dielectric interfaces. As mentioned before, despite of the progress made in the modification of thermal boundary conductance, systematic ways to properly modify boundary conductance in presence of an interlayer at any metal-dielectric interface is still not well understood. In this thesis, we did a systematic study of the effect of an interlayer on interfacial thermal transport in perspective of three parameters electron-phonon coupling constant (g), Debye temperature (θ_D), and acoustic phonon cut-off frequency (v_L, v_T). The factors such as interface roughness, grain boundaries, interfacial defects, and interfacial bonding that determine the interfacial quality are difficult to control and characterize, and hence we are not analyzing them in this study. We are concerned with interlayer thickness less than 10 nm because most of the modifications or changes to thermal boundary conductance happen within the initial few nanometers before reaching a saturation [13], [14]. For applications such as plasmonic devices, it is important to maximize heat dissipation without introducing materials that give rise to optical losses, so interlayer thicknesses need to be as small as possible.

This thesis is organized into six chapters. Chapter 2 describes the experimental methods used for measuring the thermal properties of materials. We use a typical time domain thermoreflectance experimental set-up to measure the heat transport properties. The experimental

set-up is described in detail here. Chapter 3 contains details about the theoretical modeling of the thermal boundary conductance. We use a modified diffuse mismatch model to get the phonon contribution of thermal boundary conductance at a metal-dielectric system. Mathematical description of other scattering processes is also included. In Chapter 4, we study the size effects of the interlayer at metal-dielectric interfaces. We analyze the modification of the thermal boundary conductance at metal-dielectric interfaces by insertion of metal interlayers with thicknesses varying between 0.25 nm and 10 nm. The results show that the resistance due to electron-phonon coupling in interlayer has a profound role in determining the thickness dependence trend of thermal boundary conductance. In Chapter 5, we analyze the various factors that contribute to the boundary conductance modification with addition of a 5 nm interlayer. We show that the overlap between vibrational spectra of metal-interlayer-substrate system and electron-phonon coupling strength in metal and interlayer plays a vital role in modifying the interfacial thermal transport. Chapter 6 concludes the thesis.

CHAPTER 2

EXPERIMENTAL TECHNIQUES

2.1 Time-domain thermoreflectance

The characterization of thermal transport based on ultrafast lasers allows temperature measurements at time scales comparable to the relaxation time of energy carriers (electrons and phonons) [38]. Time-domain thermoreflectance (TDTR) is an effective tool for measuring such ultrafast thermal transports. TDTR is a pump-probe technique that uses a femtosecond laser to measure the temperature dependence of optical reflectivity as a function of time in materials [39]–[41].

A typical TDTR set-up uses a modulated pump beam to heat up sample surface; consequently, a probe beam applied at the same position on sample probes the change in reflectivity. Relative arrival time of pump and probe beam is controlled by placing a delay stage either in the pump or probe path. Constant speed of light helps in achieving a time delay by adjusting the beam path length by moving the position of the delay stage. TDTR measures the change in reflectance (thermoreflectance signal) of the sample given by:

$$\Delta R = \frac{dR}{dT}\Delta T \qquad (8)$$

where, ΔT is the change in surface temperature and $\frac{dR}{dT}$ is the thermoreflectance coefficient [42]. The thermal properties can be extracted from the thermoreflectance signal by fitting the experimental data to a known thermal model.

Measurement of thermal properties using pump-probe system was developed during 1970s and 1980s. Initially, in 1986 Paddock and Eesley [43] constructed a pump-probe system to measure thermal diffusivity of metal films using picosecond time-resolved thermoreflectance method. Several modifications were done to this technique over the past few decades to measure thermal properties [41], [44]–[47]. Cahill's group in 2003 developed an advanced pump-probe system, which included several new features such as a CCD camera for visualizing pump and probe beams, and an objective lens for focusing pump and probe beams. Further, in 2008, Schmidt [39] developed a system incorporating the above features with some additional improvements. Some of the new features in Schmidt's system were the following: a frequency doubled pump beam which reduced the optical noise and allowed for a simplified coaxial geometry, and a beam expander in the probe beam path to reduce the beam divergence over the delay stage.

We have constructed a pump-probe experimental set-up (Fig. 2.1) similar to the system developed by Schmidt. Detailed information about the design and optics of the pump-probe system can be found in Ref. [39]. We use an ultrafast fiber laser that generates pulses at 1030 nm with a pulse width of ~300 fs at a repetition rate of 40 MHz. The probe beam is at 1030 nm and pump beam has been frequency doubled from 1030 nm to 515 nm. The electro-optic modulator (EOM) in the pump path imposes a square wave modulation at ~1 MHz (This usually varies between 1-3.5 MHz in our experiments and is controlled by a function generator). The modulated pump pulse generates a temperature rise on the surface of the sample at the frequency of the EOM. The probe beam passes through a beam expander to reduce the beam divergence at long time delays. Less than 5% change in probe radius over the 4 ns delay stage was achieved with beam expander. A mechanical delay stage (0-4 ns) in the probe path controls the arrival time of the probe beam with respect to pump at the sample. The probe and pump beams are then focussed collinearly to the

sample surface through a long working distance 4X objective. The sample is mounted on a stage which can be moved so that the pump and probe beams are in focus at the sample surface.

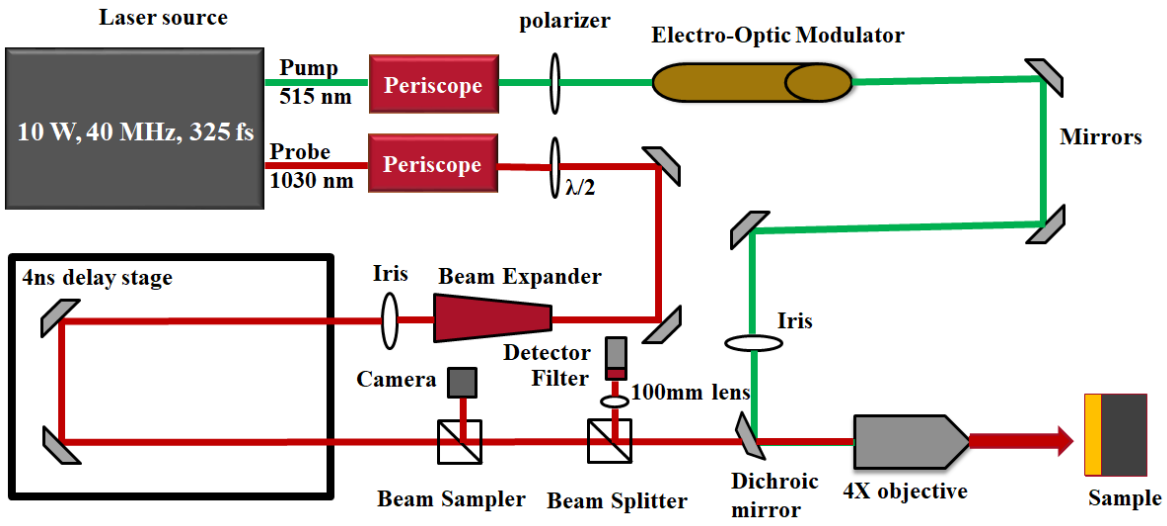

Fig. 2.1. Schematic diagram of experimental set-up

When the sample is at focus, the reflected probe beam emerges collimated from the objective. The probe beam measures the change in reflectivity at the sample surface. A 50:50 beam splitter placed in the probe path directs the reflected pump and probe into a camera and a detector. The camera helps in visualizing the pump and probe beams. The detector detects the reflected probe beam intensity and a lock-in amplifier (HF2LI - Zurich Instruments) records the amplitude and phase of the thermoreflectance signal. We used an InGaAs biased detector (DET10N - Thorlabs) with a rise time of 5 ns. Detection of the reflected modulated pump beam is blocked by an optical filter placed in front of the detector. For a typical transducer (such as Al, Au), the thermoreflectance coefficient value is very low (~10^{-4} - 10^{-5} K^{-1}), hence a tiny amount of reflected pump beam significantly

distorts thermoreflectance signal. A lock-in amplifier based detection helps in improving the signal to noise ratio by extracting the thermoreflectance signal at a specific reference frequency (frequency of EOM) from the noisy background. The lock-in amplifier sampling-rate was set at 225 Hz and we used a filter slope of 48 dB/Oct with 1 s time constant to enhance the signal to noise ratio. The lock-in amplifier provides two outputs, an in-phase signal (V_{in}, *real part*) and an out of phase signal (V_{out}, *imaginary part*) at the modulation frequency. The amplitude (V), phase (φ), and ratio (R) of the signal can be calculated as $\sqrt{V_{in}^2 + V_{out}^2}$, $\tan^{-1}(V_{out}/V_{in})$, and $-V_{in}/V_{out}$ respectively. We use the phase of the thermoreflectance signal to extract thermal properties because the phase has a ratio of the in-phase and out-of-phase signals; hence, it does not need

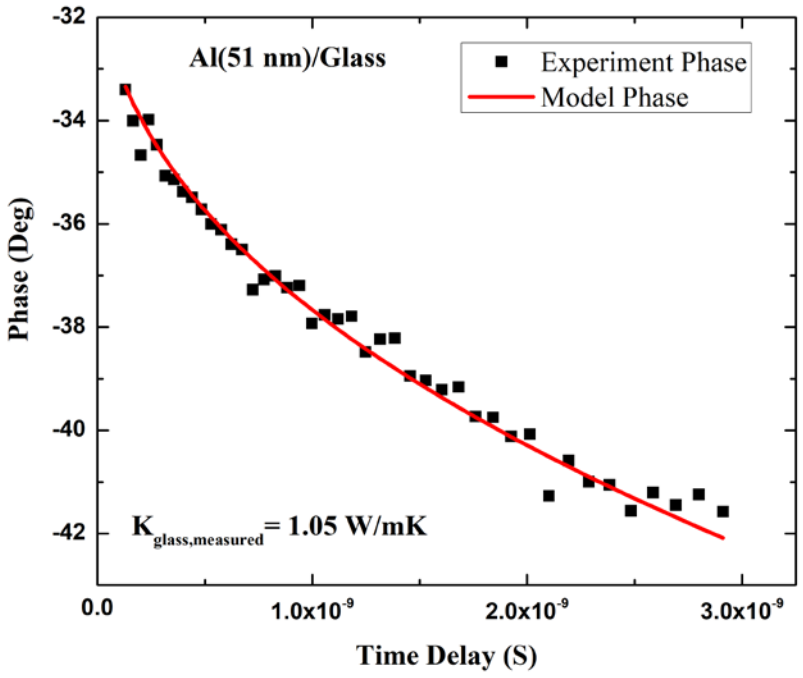

Fig. 2.2. Shows the phase data and best-fit value for 51nm Al on glass. The red curve represents the phase calculated from thermal model and the black squares represent the experimental data. The $k_{glass,measured}$ represents the measured glass thermal conductivity.

normalization. Noise in both components due to fluctuations in laser power also cancels out. The phase shift introduced due to electrical components (cables, electrical, and optical components) in the TDTR experiments can be compensated due to the fact that V_{out} signal should remain unchanged at zero time delays [39].

Knife edge method [39] was used to measure the pump and probe spot sizes. The $1/e^2$ pump radius was measured to be ~7.5 μm. The $1/e^2$ radius of the probe beam is ~4 μm when the delay stage is at 1 ns time delay and ~4.2 μm when the delay stage is at 4 ns time delay. Beam divergence at higher time delays was reduced using the beam expander.

2.2 Data analysis and post-processing

In order to obtain quantitative results for thermal conductivity and interface thermal conductance, we compare the experimental results (i.e. phase of thermoreflectance signal) with a theoretical thermal transport model as shown in Fig. 2.2. Fig. 2.2 shows the phase data and the best fit for the measured thermal conductivity of glass coated with 51 nm Al. We adjust the unknown fitting parameters until the experimental data and model match. We use the thermal model developed by Cahill (see section 2.2.1), which is based on the solution to the heat diffusion equation for a periodic point source (i.e. the laser) on a semi-infinite anisotropic layered media [48].

2.2.1 Modeling heat transport in multilayers for TDTR

Cahill's thermal model [48] is based on Feldman's algorithm [49] for one-dimensional heat diffusion through layered structures. They extended the algorithm to solve for TDTR thermal

response in a three-dimensional layered structure. The solutions to transient heat diffusion equation calculated in frequency domain (both time and space) for an n-layer model is used as an input for in-phase and out-of-phase lock-in amplifier thermoreflectance signals written in terms of frequency components.

The frequency-domain solution to the temperature distribution on the surface of a semi-infinite solid can be expressed as a spherical thermal wave,

$$g(r) = \frac{exp(-pr)}{2\pi kr} \quad (9)$$

with, $p^2 = \frac{i\omega}{D}$, ω being the angular frequency, D the thermal diffusivity, k the thermal conductivity and r the radial coordinate. The Hankel transform of Eq. 9 on r gives the surface temperature as:

$$G(s) = \frac{1}{k(4\pi^2 s^2 + p^2)^{1/2}} \quad (10)$$

This transformation is useful for analysis in Fourier space in radially symmetric systems. The Hankel transform of a Gaussian heat source (pump beam) with radius w_0 and amplitude A is given by:

$$H(s) = Ae^{\left(\frac{-\pi^2 s^2 w_0^2}{2}\right)} \quad (11)$$

The inverse transform product of $G(s)$ and $H(s)$ gives the surface temperature distribution as:

$$\theta(r) = 2\pi \int_0^\infty G(s)H(s)J_0(2\pi sr)s\, ds \quad (12)$$

The weighted average of temperature distribution measured by a Gaussian probe beam with radius w_1 is given by:

$$\Delta T = 2\pi A \int_0^\infty G(s)e^{\left(\frac{-\pi^2 s^2 (w_0^2 + w_1^2)}{2}\right)} s\, ds \quad (13)$$

Eq. 13 gives the surface temperature on a semi-infinite solid. For layered materials, the surface temperature on layer *n* with thickness L_n, diffusivity D_n, and thermal conductivity k_n is related to the adjacent layer *(n+1)* by [48], [49],

$$\begin{pmatrix} B^+ \\ B^- \end{pmatrix}_n = \frac{1}{2\gamma_n} \begin{pmatrix} exp(-u_n L_n) & 0 \\ 0 & exp(u_n L_n) \end{pmatrix} \begin{pmatrix} \gamma_n + \gamma_{n+1} & \gamma_n - \gamma_{n+1} \\ \gamma_n - \gamma_{n+1} & \gamma_n + \gamma_{n+1} \end{pmatrix} \begin{pmatrix} B^+ \\ B^- \end{pmatrix}_{n+1} \quad (14)$$

$$u_n = (4\pi^2 s^2 + p_n^2)^{1/2} \quad (15)$$

$$p_n^2 = \frac{i\omega}{D_n} \quad (16)$$

$$\gamma_n = k_n u_n \quad (17)$$

Since the final layer is semi-infinite, and the modulated heat source cannot reach the far end of final layer, B^+=0 and B^-=1. The interface is modeled as a thin layer with a small thickness and heat capacity. The frequency-domain thermal response for a layered structure is given by:

$$\Delta T = 2\pi A \int_0^\infty \left(\frac{B_1^+ + B_1^-}{B_1^+ - B_1^-}\right) \frac{1}{\gamma_1} e^{\left(\frac{-\pi^2 s^2 (w_0^2 + w_1^2)}{2}\right)} s \, ds \quad (18)$$

The lock-in amplifier measures the in-phase and out-of-phase components of the signal ΔT at a particular modulation frequency and time delay. The in-phase and out-of-phase components in frequency-domain measured by the lock-in amplifier evaluated at the modulation frequency *f* and *–f* is given by [48],

$$Re[\Delta R_M(t)] = \frac{dR}{dT} \sum_{m=-M}^{M} (\Delta T(m/\tau_r + f) + \Delta T(m/\tau_r - f)) exp(i2\pi m t/\tau_r) \quad (19)$$

$$Im[\Delta R_M(t)] = -i \frac{dR}{dT} \sum_{m=-M}^{M} (\Delta T(m/\tau_r + f) - \Delta T(m/\tau_r - f)) exp(i2\pi m t/\tau_r) \quad (20)$$

$\frac{dR}{dT}$ is the change in reflectivity with surface temperature, τ_r is the repetition rate of laser, t is the time delay between pump and probe, and ΔT is the solution to the surface temperature distribution in frequency domain (Eq. 18 and 13). As mentioned before, the phase of the thermoreflectance signal can be calculated from Eq. 19 and 20 as:

$$\varphi = tan^{-1}\left(Im[\Delta R_M(t)] \Big/ Re[\Delta R_M(t)]\right) \quad (21)$$

The data acquisition in TDTR is done by repeated lock-in measurements at different time delays. Eq. 21 is then fitted with the experimental phase data to extract the thermal properties.

2.2.2 Measurement of thermal properties

Fig. 2.3 shows a typical TDTR plot for a 50 nm Al on MgO sample. The TDTR plots give information about different time regimes. The laser energy is initially absorbed at the metal surface. Within the initial ~10 ps during and after the light absorption, electron-electron thermalization happens, and they exchange the remaining energy with the cold lattice (here, Al lattice). In the following 10-100 ps, due to the rapid laser pulse heating, a strain wave propagates through the metal and reflects back from the interface at the speed of sound. This can be observed as periodic oscillations in the TDTR signal (Fig. 2.6). The signal decays as the heat diffuses from the metal layer to the substrate via phonon-phonon and electron-phonon interactions. In order to extract thermal properties such as thermal conductivity (k) of materials and thermal boundary conductance (G), the TDTR data taken up to higher pump and probe time delays (~3-4 ns) are fitted by the thermal transport model.

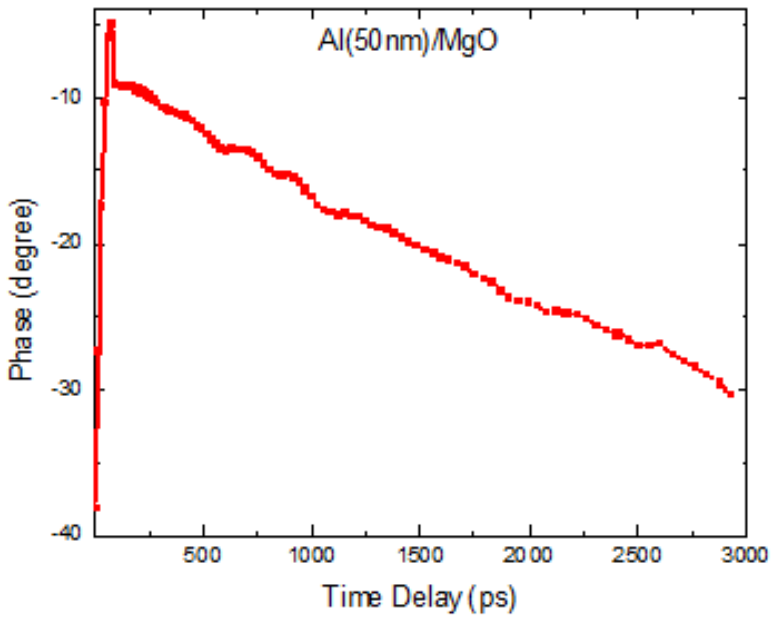

Fig. 2.3. TDTR signal for 50 nm Al on MgO

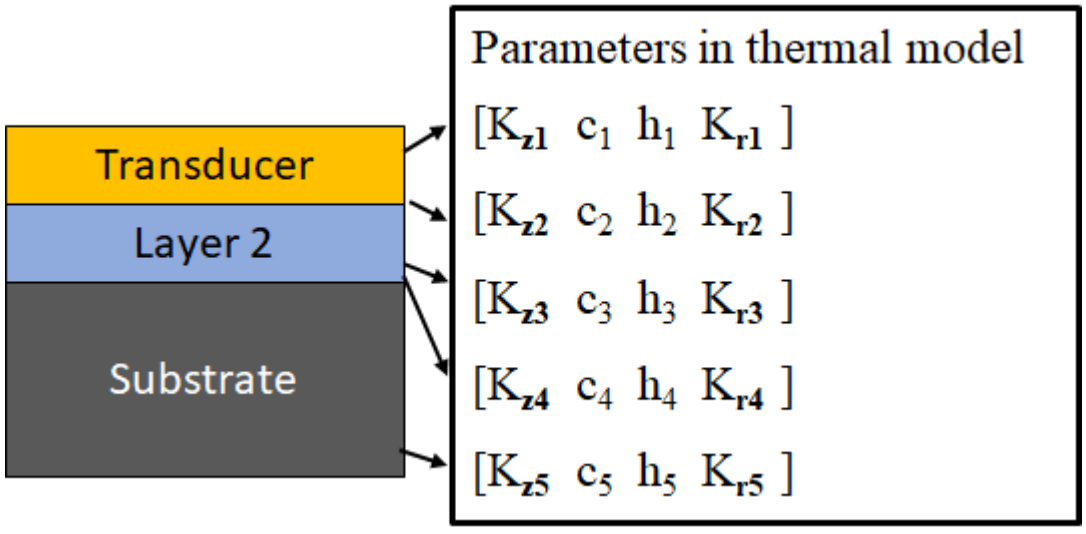

Fig. 2.4. Input parameters to the TDTR thermal model. The numbering represents the five layers in model. K_z, c, h, and K_r represents the cross-plane thermal conductivity, heat capacity, thickness, and in-plane thermal conductivity of the five layers respectively.

Fitting the thermal model with experimental data requires the knowledge of various thermophysical properties. The unknown parameters (such as G or k) can then be extracted from the fit results. Depending on the number of layers in the thermal model (interface is treated as a layer), the number of input parameters may vary (Fig. 2.4). Fig. 2.4 shows a 5-layer model (3 materials and 2 interfaces) with various input parameters. The thermal response at the sample surface depends on modulation frequency (f), repetition rate of laser (τ_r), pump (w_0) and probe (w_1) diameters, thermal conductivity (in-plane (k_r) and out-of-plane (k_z)), volumetric heat capacity (c), and film thickness (h) of each material in the sample. The thermal boundary conductance G can be expressed as a ratio of thermal conductivity over the thickness of the layer describing the interface. TDTR uses a top metal film as a temperature transducer layer due to the temperature dependence of optical reflectivity. A good transducer should be optically thick enough (~40 nm-60 nm) to prevent the transient reflectance signal from the substrate interfering with the transducer signal. In addition to this, transducer should have a high thermoreflectance coefficient value at the probe wavelength. Aluminum (Al) is a very common transducer layer in TDTR experiments because Al has a large thermoreflectance coefficient value in IR range at room temperature [42]. The in-plane thermal conductivity (k_r) of the transducer layer can be obtained from Wiedmann-Franz law, which relates the electrical conductivity and thermal conductivity. Electrical conductivity measurements can be performed using four-point probe technique. All other values needed in thermal model for different layers are taken from literature. In usual TDTR experiments, the usual unknown quantities are G, k_z, *and* k_r, and if the sample is isotropic, k_r and k_z reduce to a scalar quantity, k.

The thermal penetration depth is defined as the depth at which the temperature inside the materials drops to 1/e of the temperature at surface. Thermal penetration depth in a sample modulated at frequency *f* is given by:

$$d = \sqrt{\frac{k_z}{\pi c f}} \tag{22}$$

For a modulation frequency of 1 MHz, penetration depth in silicon is ~5 μm, whereas in sapphire it is ~2 μm. Laser spot size and thermal penetration depth are two important length scales in TDTR experiments. In typical TDTR experiments, the laser spot size is kept much larger than the thermal penetration depth so that the resulting thermal transport is one-dimensional along the cross-plane direction. Under such a configuration, the experiments are more sensitive to out-of-plane thermal conductivity and thermal boundary conductance. When the laser spot size is comparable to that of thermal penetration depth, thermal transport is predominantly three-dimensional [47]. Heat transport, in this case, is sensitive to both in-plane (k_r) and out-of-plane (k_z) thermal conductivities. TDTR can be employed on a range of materials from bulk to nanoscale. However, in the case of nanoscale materials, TDTR cannot be used to measure *thermally thin* materials (*film thickness* < *d*) due to low sensitivity to the out-of-plane thermal conductivity. Nanomaterials must be *thermally thick* (*film thickness* > *d*) for performing TDTR measurements; i.e., the thermal penetration depth should be smaller than the thickness of the film.

It should be noted that, despite the large number of input parameters, thermal model is not sensitive to all of them. Sensitivities of various parameters to the thermal model can be determined quantitatively. The sensitivity of phase (φ) to an input parameter *x* in layer *n* can be defined as:

$$S_{x_n} = \frac{d\varphi}{d\ ln\ x_n} \tag{23}$$

Fig. 2.5 shows the phase sensitivity for 10% change in two parameters in-plane (k_r) and out-of-plane (k_z) thermal conductivities for Al (53 nm)/Sapphire sample. k_{z1}, k_{z2}, k_{z3}, k_{r1}, k_{r2}, and k_{r3} represent the cross-plane and in-plane thermal conductivities in Al, Al/sapphire interface and sapphire, respectively. The plot clearly shows that the in-plane thermal conductivities have zero sensitivity, which indicates that even a large change in k_r makes no difference in TDTR measurements. As mentioned earlier, TDTR measurements are not sensitive to in-plane thermal conductivities due to relatively large spot sizes. Hence, with the current configuration, it is difficult to accurately determine those parameters from the fit. TDTR measurement for this sample is most sensitive to sapphire thermal conductivity (k_{z3}) and interfacial thermal conductivity (k_{z2}). Sensitivities for k_{z3} and k_{z2} decreases with increasing time delay.

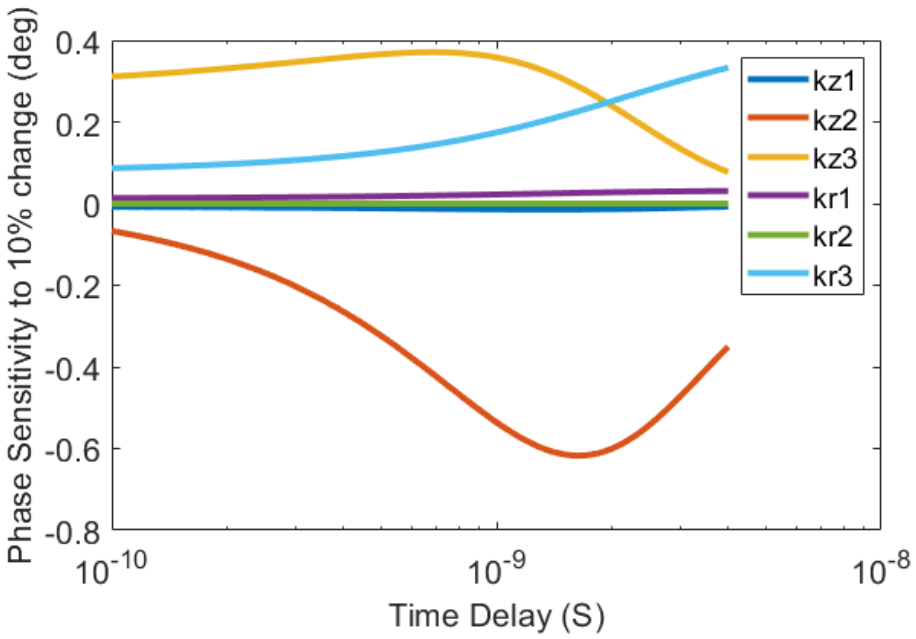

Fig. 2.5. Sensitivity plot for Al (53 nm)/sapphire as a function of time delay.

2.3 Picosecond Acoustics

Picosecond acoustics is a technique used to accurately measure thickness of thin films, and here it will be used to accurately measure the transducer layer. As mentioned before, at lower time delays (~10-100 ps) the TDTR signal has acoustic echoes due to the instantaneous absorption of laser energy. When the laser energy is absorbed at the sample surface, the lattice expands quickly due to the rapid increase in temperature resulting in the propagation of a sound wave through the transducer. This sound wave is partially reflected at the interface between the transducer and the substrate due to an abrupt change in acoustic impedance. The wave then returns to the sample surface after time $\tau = \frac{2h}{V_s}$, where h is the thickness of the transducer layer and V_s is the speed of sound in transducer. When the wave returns to the surface reflectivity changes due to the strain at the surface. Optical reflectivity changes due to the change in density, which in turn modifies the optical reflectivity coefficient.

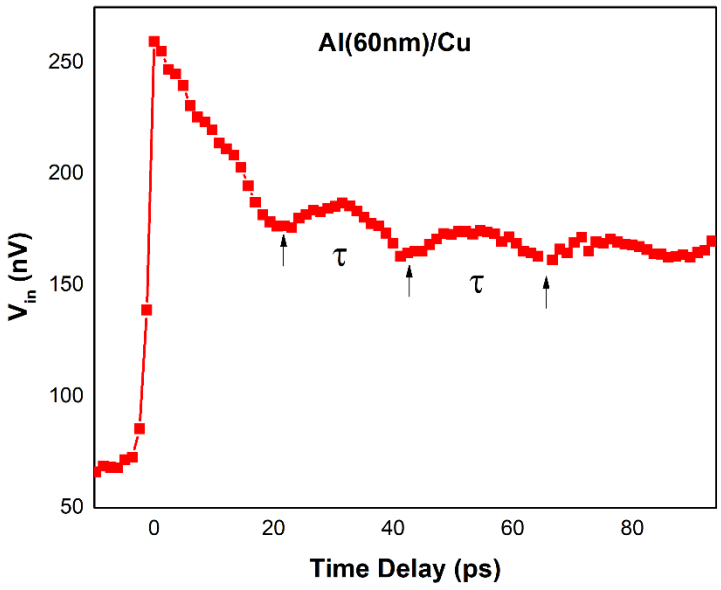

Fig. 2.6. Acoustic echoes on a 60 nm Al film on Cu substrate

Fig. 2.6 shows the acoustic echoes on a 60 nm Al film on a Cu substrate. From the figure, τ can be estimated to be ~20 ps. Since the speed of sound in Al is known to be 6260 m/s, we can accurately determine the thickness of the Al to be 60 nm film using:

$$h = \frac{1}{2} t_{echo} V_s \quad (24)$$

2.4 Sample Preparations

2.4.1 Samples for interlayer thickness-dependent G analysis

We deposited Al and interlayers (Ni and Ta) on c-sapphire (0001) and Si substrate by dc magnetron sputtering in an argon atmosphere with a base pressure at ~ 1×10^{-7} Torr at 200 W. Deposition rates for Al, Ni and Ta are 1.1 $Å s^{-1}$ at 3 mTorr 1.4 $Å s^{-1}$ at 3 mTorr and 1.8 $Å s^{-1}$ at 3 mTorr respectively. Prior to the metal bilayer deposition, substrates were cleaned by sonicating in acetone and isopropanol (~10 min each) using an ultrasonic bath. Thickness of the metal bilayers were estimated using picosecond acoustics and profilometry. Thermal properties of the metal-interlayer-substrate system were measured using a time domain thermoreflectance set-up. Details of the interlayer thickness-dependent G study can be found in Chapter 4.

2.4.2 Samples for the analysis of heat transport mechanisms

The metal bilayers were deposited on substrate using magnetron sputtering. For the samples on AlN, 1μm AlN was epitaxially grown on a sapphire substrate by the substrate vendor. The metal layers were then sputter deposited on top of the AlN. X-ray reflectivity (XRR) was used

to measure the thickness of the deposited metal bilayers. We used time-domain thermoreflectance to measure the thermal transport properties in the above samples. For these samples, sputter deposition and XRR was done by the Hellwig group at Technische Universität Chemnitz and Helmholtz-Zentrum Dresden-Rossendorf. Details of the study on various heat transport mechanisms in the presence of an interlayer can be found in Chapter 5.

CHAPTER 3

MATHEMATICAL MODELING OF INTERFACIAL THERMAL TRANSPORT

In this section, we focus on mathematical modeling of interfacial heat transfer, which predicts the thermal boundary conductance based on different scattering events. The two theoretical models widely used for predicting the phonon contribution of boundary conductance are: (a) acoustic mismatch model (AMM) and (b) diffuse mismatch model (DMM). AMM and DMM differ in the assumption made on phonon scattering at the interface. AMM assumes a flat interface, and the incoming phonon flux from material *A* undergoes specular reflection and transmission [50]. AMM treats phonons as a plane wave, and the transmission probabilities can be determined from a model analog to Snell's law for electromagnetic waves. When the phonon wavelength is much larger than interface roughness, phonon transmission probability with frequency ω from material *A* to *B* can be expressed as [50]:

$$\alpha_{A\to B}(\omega, i, q) = \frac{4Z_A Z_B \mu_A \mu_B}{(Z_A \mu_A + Z_B \mu_B)^2} \qquad (25)$$

where, Z is the acoustic impedance, and $\mu = cos\ \theta$, where θ is the phonon angle of incidence measured from normal to the surface. Transmission probability $\alpha_{A\to B}(\omega, i, q)$ depends on both the phonon polarization *i* and wavevector q. The thermal boundary conductance can then be calculated using:

$$G_{pp,AMM} = \frac{1}{4}\sum_{q,i}\int_0^{\omega_c(i,q)} \hbar\omega \ \ |v_A(\omega, i, j)| D_A(\omega, i, q)\alpha_{A\to B}(\omega, i, q)\frac{df_{BE}}{dT}\, d\omega \qquad (26)$$

Here, ω_c is the maximum phonon frequency, $D_A(\omega, i, q)$ is the phonon density of states of material A, $\upsilon_{\mathrm{A}}(\omega, i, j)$ is the phonon velocity in material A, and f_{BE} is the Bose-Einstein distribution function. AMM is only valid for low-frequency phonons (less than 100 GHz) [50]. Because it assumes a plane interface, when the phonon wavelengths are short enough to be comparable to that of interfacial roughness, AMM cannot accommodate for them. It has been shown from various experiments that thermal boundary conductance can be predicted accurately by AMM at low temperatures (less than 1 K) [50]. In short, AMM describes phonon scattering at low temperatures when the wavelength of incident phonon is larger than interface roughness.

DMM, on the other hand, assumes diffusive scattering across the boundary [28]. Under this assumption, incoming phonons from material *A* scatters diffusively and loses memory of the acoustic correlations (direction and mode) between the incoming and outgoing phonons. Thus, the phonon transmission probability is only determined by the phonon properties of material *A* and *B*. DMM can predict the interfacial thermal conductance at higher temperatures (T greater than 15 K). As the temperature approaches room temperature, DMM has shown to underestimate or overestimate experimental boundary conductance. To tackle this problem, there are different modified DMM approaches that account for other relevant phonon properties and mechanisms [51]–[53]. For example, using real phonon dispersions [51], [52], accounting for electron-phonon coupling strength [21], contribution to inelastic scattering [53]–[55], considering anisotropy in materials [56], and considering optical phonon contribution [57], have shown to reduce the disagreement between experiment and DMM values. A detailed description of various DMM models based on different scattering mechanisms is available in Ref. [58]. In practice, all DMM models have a limited ability to predict experimental values due to other contributions that are not built in the model, such as interface roughness and bonding.

In this chapter, we analyze various scattering mechanisms that contribute to the overall thermal conductance at a metal-dielectric interface. We analyze diffuse mismatch models developed assuming different scattering mechanisms at the interface. Later the results from the modeling are used for checking agreement with experimental thermal boundary conductance. In all DMM calculations, we assume an isotropic phonon dispersion along crystal growth direction and use realistic phonon dispersion relations. Assuming an isotropic phonon dispersion makes the computation much easier and is a good enough approximation of the three-dimensional phonon dispersion with cubic BZ systems [52]. *G* calculation using a Debye approximation (linear dispersion relation) tends to overestimate the thermal boundary conductance. Hence, a good approach to tackle this is to use a realistic phonon dispersion which shows better agreement to the experiments [51].

3.1 Diffuse Mismatch Model

3.1.1 Elastic phonon scattering assumption

In this case, the incoming phonon flux from material *A* is assumed to scatter elastically at the interface; that is, phonons with frequency ω in material *A* can only emit phonons of frequency ω from the interface. Phonon flux from material *A* approaching material *B* [59] is represented by:

$$J_{A\to B} = \frac{1}{8\pi^3}\sum_j \int_{q_{x,A}} \int_{q_{y,A}} \int_{q_{z,A}} \hbar\omega_A f_{BE} v_{j,A} dq_{x,A} dq_{y,A} dq_{z,A} \qquad (27)$$

Here, q is the wavevector, ω_A is the angular frequency of phonons, f_{BE} is the Bose-Einstein distribution function, v is the phonon group velocity, and j is the phonon polarization. Assuming

an isotropic dispersion and using the principle of detailed balance [58], transmission probability can be expressed as:

$$\alpha_{A\to B} = \frac{\sum_{j,B} \hbar\omega_{j,B} q_{j,B}^2 \upsilon_{j,B} f_{BE} dq_{j,B}}{\sum_{j,B} \hbar\omega_{j,B} q_{j,B}^2 \upsilon_{j,B} f_{BE} dq_{j,B} + \sum_{j,A} \hbar\omega_{j,A} q_{j,A}^2 \upsilon_{j,A} f_{BE} dq_{j,A}} \quad (28)$$

Total thermal boundary conductance can be expressed as a first order derivative of total heat current density with respect to temperature,

$$G_{pp} = \frac{1}{8\pi^2} \sum_{j,A} \int_{k_{j,A}} \hbar\omega_{j,A} q_{j,A}^2 |\upsilon_{j,A}| \alpha_{A\to B} \frac{df_{BE}}{dT} dq_{j,A} \quad (29)$$

3.1.2 Inelastic phonon scattering assumption

Several experimental results have shown that when there is a large acoustic mismatch, elastic DMM underestimates the interfacial conductance [37]. One way to address this problem is to account for the inelastic scattering processes at interface. In the inelastic phonon scattering assumption, phonons of all frequency in material *A* participate in the scattering process [37]. Phonons with a frequency ω_1 in material *A* emits several phonons of frequency ω_2 from the interface. For example, in three phonon inelastic process, a high-frequency phonon $\omega 1$ breaks down into two low-frequency phonon $\omega 2$ and $\omega 3$; this inelastic process can be expressed as $\omega 1 = \omega 2 + \omega 3$ or $2\omega = \omega + \omega$. Transmission probability can be expressed as [53]:

$$\alpha_{A\to B} = \frac{\sum_{j,B} \int_{q_{j,B}} \hbar\omega_{j,B} q_{j,B}^2 \upsilon_{j,B} f_{BE} dq_{j,B}}{\sum_{j,B} \int_{q_{j,B}} \hbar\omega_{j,B} q_{j,B}^2 \upsilon_{j,B} f_{BE} dq_{j,B} + \sum_{j,A} \int_{k_{j,A}} \hbar\omega_{j,A} q_{j,A}^2 \upsilon_{j,A} f_{BE} dq_{j,A}} \quad (30)$$

The total interfacial thermal conductance can be calculated using Eq. 29.

3.2 Electron-phonon coupling contribution

In a metal-dielectric system, the contribution to conductance from electron-phonon interaction in metal is given by [21]:

$$G_{ep} = \sqrt{k_p g} \tag{31}$$

Phonon thermal conductivity (k_p) can be estimated by kinetic theory– $k_p = v_s \Lambda_p c_p/3$, where c_p is the volumetric heat capacity of phonons, $\Lambda_p$is the mean free path of phonons, and v_s is the velocity of sound.

Volumetric electron-phonon coupling constant g describes energy exchange between electrons and phonons. Typical values for the volumetric electron-phonon constant at room temperature is in the order of 10^{16} - 10^{18} $Wm^{-3}K^{-1}$.

3.3 Electron-electron contribution

Thermal conductance at the interface between two metals due to electron-electron interaction can be expressed as [60]:

$$G_{ee} = \frac{\gamma_{e,A} v_{e,A} \gamma_{e,B} v_{e,B}}{4(\gamma_{e,A} v_{e,A} + \gamma_{e,B} v_{e,B})} T \tag{32}$$

with $\gamma_{e,i} = C_{e,i}/T$ being the Sommerfeld parameter, and $v_{e,i}$ being the fermi velocity.

3.4 Two-temperature model

As mentioned before, energy carrier relaxation mechanisms in a metal-dielectric system during and after ultrafast heating involve different pathways (Fig. 1.2). Two-temperature model (TTM) describes the interaction of the ultrafast laser heating with free electrons and its consequent cooling by exchanging energy with the lattice. In metals, during an ultrafast heating process, the free electrons absorb the incident photons, raising the material's temperature by few thousand Kelvin. Electron distribution cannot be predicted by Fermi-Dirac distribution in this highly non-equilibrium state. In TDTR experiments, this is observed as a rapid rise in signal. Further, these hot electrons simultaneously undergo electron-electron collisions and ballistic electron transport in the metal film. Within few hundreds femtoseconds (~ < 500 fs), hot electrons thermalize and can be defined by an electron temperature (T_e). Due to the small volumetric specific heat of electrons (~ 10^4 J/m^{2}K) this temperature will be much higher than the cold lattice. Energy exchange between electrons and lattice takes place via electron-phonon scattering events. This process slowly increases the lattice temperature. For a bimetallic system, this transport process can be modeled using two coupled nonlinear equations [61], [62]:

$$c_e(T_e)^{(1,2)}\frac{\partial T_e^{(1,2)}}{\partial t} = k_{e1,2}(T_e)\frac{\partial^2 T_e^{(1,2)}}{\partial z^2} - g_{1,2}(T_e^{(1,2)} - T_i^{(1,2)}) \quad (33)$$

$$c_i(T_i)^{(1,2)}\frac{\partial T_i^{(1,2)}}{\partial t} = g_{1,2}(T_e^{(1,2)} - T_i^{(1,2)}) \quad (34)$$

Here, T_e and T_i are the electron and phonon temperatures, c_e and c_i are the volumetric heat capacities of electrons and phonons, k_e is the electron thermal conductivity, and g is the electron-phonon coupling constant. Superscripts 1 and 2 represent two metallic layers. Eq. 33 and 34 represent the temporal and spatial electronic (after electron thermalization) and phononic

temperature evolutions in one dimension. Applying proper boundary conditions, *Te* and *Ti* can be determined to be [61]:

$$T_e(\omega, z=0) = \frac{(1-R)IF(\omega)}{\sqrt{k_1 g_1}+\sqrt{k_2 g_2}} \left(\frac{1}{1+\frac{\sqrt{k_2 g_2}-\sqrt{k_1 g_1}}{\sqrt{k_2 g_2}+\sqrt{k_1 g_1}} e^{-2L/\sqrt{k_1 g_1}}} \right) e^{-L/\sqrt{k_1 g_1}} \quad (35)$$

$$T_i^{(1,2)}(z,t) = \frac{1}{(g/c_i)^{(1,2)}} \int_0^t T_e^{(1,2)}(z,t') e^{-\frac{t-t'}{(g/c_i)^{(1,2)}}} dt' \quad (36)$$

where g is electron-phonon coupling constant, c_i is the heat capacity of lattice, L is the layer thickness, R is the reflectivity coefficient, I is the laser intensity, and $F(\omega)$ is the evolution of laser pulse in frequency domain.

CHAPTER 4

TUNING THE THERMAL BOUNDARY CONDUCTANCE AT METAL-DIELECTRIC INTERFACE BY VARYING INTERLAYER THICKNESS

In this chapter, we focus on understating the interlayer size effects at the metal-dielectric interface. Quality of interface, electron-phonon coupling strength, and phonon mismatch are important factors in determining the thermal boundary conductance. Here, we analyze the modification of the thermal boundary conductance at metal-dielectric interfaces by insertion of metal interlayers with varying thicknesses in the few-nanometer range. We show that the insertion of a tantalum interlayer at Al/Si and Al/sapphire interfaces hinders the phonon transmission across those boundaries, thereby enhancing the interfacial thermal resistance across the boundary. As the tantalum thickness was increased from 0.25 nm to 10 nm, the interfacial thermal conductance decreased sharply until it plateaus at ~ 1 nm. We show that electron-phonon coupling has a major influence on thermal boundary conductance, and if the coupling strength is strong, the thickness dependent *G* saturates within 2 nm. We found that the addition of a nickel interlayer with thicknesses varying from 0.25 nm to 10 nm significantly affected thermal interfacial conductance at both the Al/Si and the Al/sapphire interfaces. We show that as the Ni interlayer thickness increases, G has a local minimum, and the less strong electron-phonon coupling in Ni causes G to saturate slowly. Thermal property measurements were performed using time domain thermo-reflectance and are in good agreement with a formulation of the diffuse mismatch model based on

real phonon dispersions, accounting for anharmonic phonon scattering and phonon confinement within the interlayer.

4.1 Introduction

Interfacial properties can be actively tuned by inserting an interlayer between the metal and the substrate. Many previous studies both theoretically and experimentally show that an interlayer has a profound influence on interfacial thermal conductance at very small thickness before it saturates. Nevertheless, factors that affect the interlayer contribution to G is still not well understood. Jeong et al. [13] showed the effect of adding an interlayer with intermediate Debye temperature between a metal and dielectric. Adding a material with intermediate Debye temperature can enhance thermal boundary conductance by bridging phonon transport (see section 1.1.3). They studied the thickness-dependent effect of Cu and Cr interlayers at Au/sapphire interface. They developed a model to predict the evolution of G as a function of interlayer thickness based on phonon-metal/phonon-dielectric transport. Their model assumed that the phonons from Au pass directly to the substrate when the interlayer thickness is smaller than phonon wavelength. On the other hand, phonons with wavelength smaller than interlayer thickness come directly from the interlayer. However, they ignored the effect of electron-phonon coupling in both metal and interlayer. Subsequently, Blank and Weber [14] studied thickness dependence of a Cu interlayer by developing a model that accounts for both phonon-phonon interaction and electron-phonon coupling in an interlayer. Combining model with the experimental data, they predicted the evolution of thermal boundary conductance with thickness in Au/sapphire, Au/diamond, and Au/Si systems.

In this work, we study the effect of a Ni and Ta interlayer at Al/sapphire and Al/Si interfaces. Ni was chosen as an interlayer because it has similar vibrational properties to that of Al but has higher electron-phonon coupling strength than that of Al. In the case of tantalum, Ta and Al have completely dissimilar vibrational properties, but Ta has a stronger electron-phonon coupling strength than both Ni and Al. Interlayer thickness for Ta and Ni were varied between 0.25 nm and 10 nm. Table 1 shows Debye temperature (θ_D), volumetric electron-phonon coupling constant (g), and vibrational cut-off frequencies for longitudinal (ν_L) and transverse (ν_T) acoustic modes for materials of interest in this study. Fig. 4.1 shows various thermal transport mechanisms at a metal-dielectric interface in the presence of an interlayer. Heat transport pathways in the absence of an interlayer is shown in Fig. 1.2. In the presence of an interlayer, additional pathways are created depending on the interlayer properties such as electron-phonon coupling strength and

Table 1: Thermophysical properties of different materials of interest in this work

Layer 1 Metals	Interlayer	Substrate
Al (Aluminum) θ_D =428K ν_L=9.6THz ν_T=5.7THz g= 0.24×10^{18}W/(m^3 ·K)	Ni θ_D =450K ν_L = 9.1THz ν_T= 4.5THz g= 1.05×10^{18} W/(m^3 ·K)	α-Al_2O_3 θ_D =1047K ν_L=10THz ν_T= 6.9THz $\nu_{optical}$=26THz
	Ta θ_D =225K ν_L=5.5THz ν_T=3.7THz, 2.6THz g= 31×10^{18}W/(m^3 ·K)	Si θ_D =640K ν_L=12THz ν_T= 4THz $\nu_{optical}$= 15.5THz

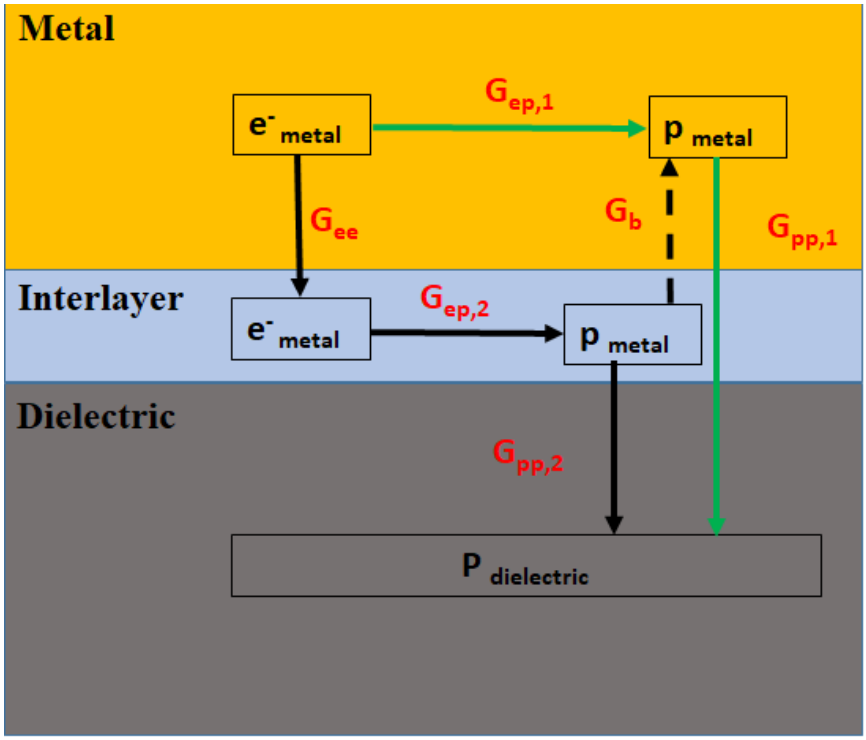

Fig. 4.1. Thermal transport mechanisms at a metal-dielectric interface in the presence of an interlayer. Green and black solid arrows represent the *pathway 1* and *pathway 2* heat transport directions respectively. Black dashed arrow represents heat backflow from interlayer to metal.

phonon spectra. The total interfacial conductance involves two parallel pathways: *pathway 1* and *pathway 2*. In *pathway 2*, since electrons carry majority of the heat in metals, the electrons in metal interact with the electrons in the metallic interlayer to transfer energy (G_{ee}). Further, interlayer electrons transfer energy to cold lattice via electron-phonon coupling ($G_{ep,2}$). Depending on the interlayer electron-phonon coupling strength, phonons from the interlayer can be transferred either to the substrate ($G_{pp,2}$) or back to the metal layer (G_b). Since thermal boundary conductance for a metal-metal system is much higher than metal-dielectric, heat transfer from interlayer to dielectric happens at a time constant ($\tau_{interface} = hc_p/G$) much larger than that of interlayer to metal. In addition to this, longer electron-phonon non-equilibrium in metal (because of smaller g) with

respect to interlayer (higher g) causes a slower rise in metal phonon temperature than interlayer lattice temperature. The faster rise in interlayer lattice temperature comparing to metal lattice temperature causes back flow of heat from interlayer to metal. This process adds another resistance pathway and decreases the overall thermal boundary conductance.

In order to analyze the effect of G_b in our current work, we performed a two-temperature model analysis in Al-Ni system (see section 3.4). Since the backpropagation only involves two metallic layers, we modeled a bimetallic structure. The temperature profile from interlayer-phonons /dielectric-phonons is not so important to analyze the back transfer (substrate matters only if it is a metal, which has a small $\tau_{interface}$ similar to the top metal). The model gives the evolution of electrons and lattice temperature rises shortly after an ultrafast laser heating. The electron-phonon coupling constant for various metals in this study follows the trend (Table 1): $g_{Ta} > g_{Ni} > g_{Al}$. Fig. 4.2 shows the electron temperature (T_e) and lattice temperature (T_i) rise in Al-Ni system as a function of time delay and thickness of metal layers. The Al layer used in this model is 50 nm thick and the interlayer is 5 nm thick. The plot clearly shows that when Al is the top metal layer, back transfer process does not happen. Due to the high g in Al the electrons and phonons transfer energy faster and both the populations reaches equilibrium within the Al layer itself. Since the Al-interlayer-substrate systems do not show any temperature rise in the interlayer, we can ignore the contribution of G_b in our calculations in this case. Further, heat from the interlayer transfers to the substrate by phonon-phonon interactions ($G_{pp,2}$). We will see that this contribution is significant in Chapter 5.

We assume that only phonons of wavelength shorter than interlayer thickness can exist in the interlayer. Interfacial conductance due to *pathway 2* (Fig. 4.1) can be expressed assuming the resistance due to all three factors are in series as:

$$\frac{1}{G_2} = \frac{1}{G_{ee}} + \frac{1}{G_{ep,2}} + \frac{1}{G_{pp,2}} \quad (37)$$

In *pathway 1*, electrons couple with the phonons in the metal ($G_{ep,1}$), and subsequently the phonons exchange energy with the substrate. Phonon from the metal layer passes directly to the substrate if the phonon wavelength is larger than the interlayer thickness ($G_{pp,1}$). Interfacial conductance due to *pathway 1* can be expressed assuming the resistances are in series as:

$$\frac{1}{G_1} = \frac{1}{G_{ep,1}} + \frac{1}{G_{pp,1}} \quad (38)$$

The calculations of contribution from individual mechanisms are explained here. To model the phonon thermal transport at the interface between metal and dielectric ($G_{pp,1}$ and $G_{pp,2}$), we use a modified diffuse mismatch model. The DMM model used in this study follows few basic assumptions, considering: (1) realistic phonon dispersion relations to calculate the transmission coefficient and *G* (2) isotropic phonon dispersion along crystal growth direction. We use different DMM scattering assumptions to check the validity of our experimental data (see section 3.1.1 and 3.1.2). Based on the assumption that phonons with wavelength less than or equal to interlayer thickness only can exist in interlayer ($h = \lambda_{max}$), the accumulation of thermal boundary conductance [40] as a function of phonon wavelength (λ) can be expressed as:

$$G_{pp,accum}(\lambda > \lambda_{min}) = \frac{1}{8\pi^2}\sum_{j,A}\int_{\lambda_{min}}^{\infty} \hbar\omega_{j,A}\alpha_{A\to B}(\lambda_{j,A})q_{j,A}^2\left|v_{j,A}(\lambda_{j,A})\right|\frac{df_{BE}}{dT}d\lambda_{j,A} \quad (39)$$

where $q = 2\pi/\lambda$ is the wavevector, $\lambda_{\min}$ represents the shortest wavelength phonon, ω_A is the angular frequency of phonons, f_{BE} is the Bose-Einstein distribution function, *v* is the phonon group velocity, and *j* is the phonon polarization. The transmission coefficient $\alpha_{A\to B}$ can be calculated based on elastic or inelastic phonon assumption using Eq. 28 and 30, respectively. The subscript *A* represents the metal. The thickness dependent $G_{pp,1}$ can be calculated using:

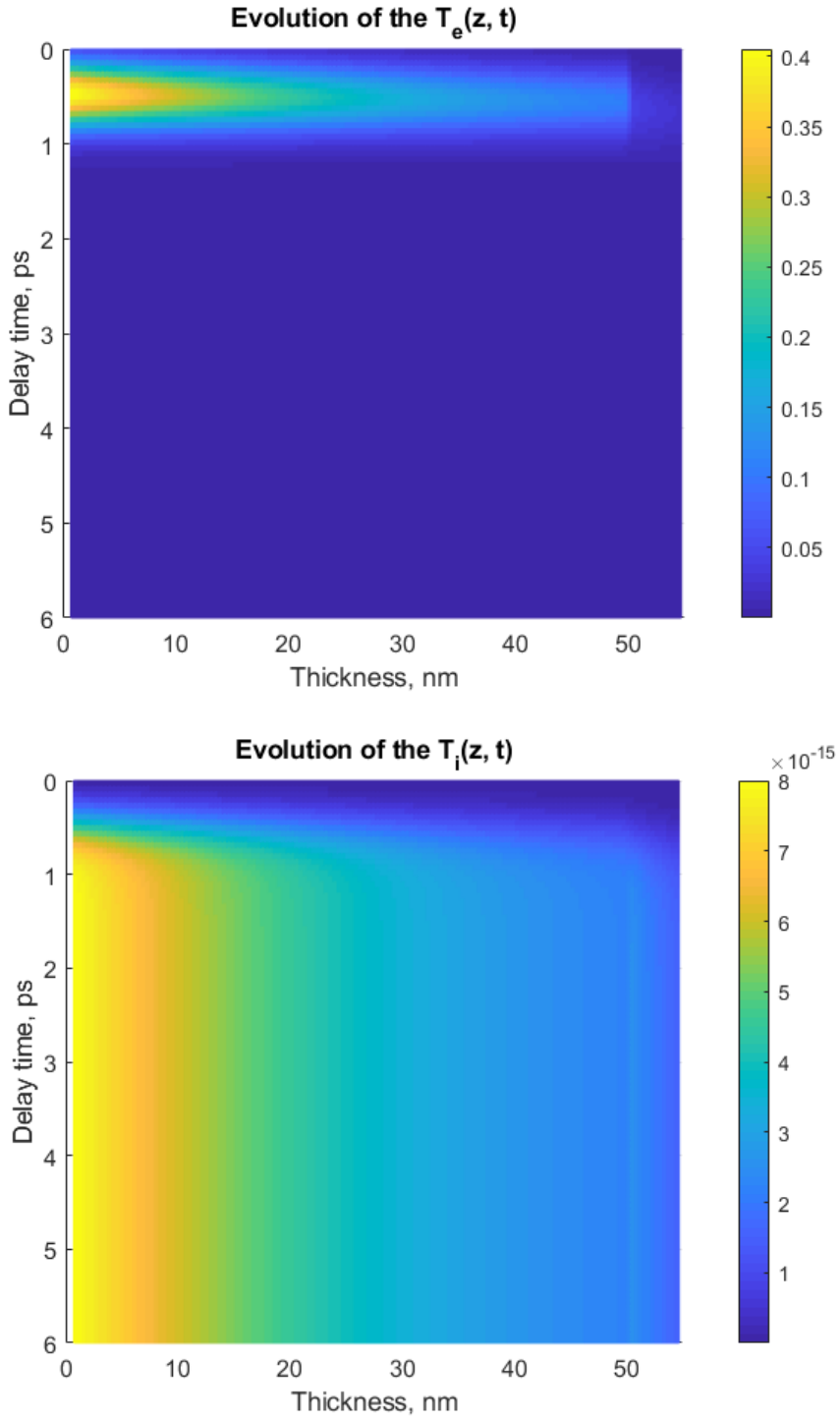

Fig. 4.2. The electronic ($T_e(z,t)$) and lattice temperature ($T_i(z,t)$) evolution as a function of delay time and two metal layer thickness in Al (50 nm)-Ni (5 nm) system. The 50 nm marks the interface between Al and Ni. The plot shows that due to relatively high g in Al the electron and phonon temperature transfers energy faster and both the population reaches an equilibrium within the Al layer itself.

$$G(\lambda)_{pp,1} = G^{metal/dielectric} - G(\lambda)_{pp,accum}^{metal/dielectric} \quad (40)$$

where, $G^{metal/dielectric}$ is the saturated value of $G(\lambda)_{\mathrm{pp,accum}}^{metal/dielectric}$. The $G(\lambda)_{\mathrm{pp},1}$is assumed to decrease with increasing thickness of interlayer (contribution from interlayer phonons increases).

The thickness-dependent resistance due to the electron-phonon coupling in interlayer with thickness *h* can be evaluated by [63],

$$G_{ep,2} = hg \quad (41)$$

This expression is valid for sub-nanometer thick layers, where electron-phonon coupling is incomplete. The contribution from electron-phonon coupling in the top metal layer (~50 nm thick) can be calculated using Eq. 31. We ignore the contribution of $G_{ep,1}$ in this calculation, due to small electron-phonon non-equilibrium (negligible resistance) in Al layer (Fig. 4.2). Adding the $G_{ep,1}$ contribution in our thermal model did not influence the results since resistance due to coupling in Al is negligible (high *g*). The contribution from electron-electron interaction (G_{ee}) is calculated using Eq. 32.

The total interfacial resistance in the presence of an interlayer can be calculated assuming the resistance due to two pathways is parallel to each other. The total contribution from each pathway can be calculated using:

$$G_{model} = G_1 + G_2 \quad (42)$$

As the interlayer thickness increases and becomes comparable to the largest phonon wavelength in interlayer, contribution from $G_{pp,1}$ in *pathway 1* becomes negligible. Long wavelength phonons (low frequency) have lesser density of states than short wavelength ones (see Fig. 5.6). Since the available phonon states are fewer, the contribution from higher wavelength phonons vanishes. In addition to this, when the top metal layer has a strong *g* (e.g. Al), the contribution from $G_{ep,1}$ in *pathway 1* is negligible (no resistance). These are the two conditions for *pathway 1* to be negligible.

4.2 Results and Analysis

We have measured the thermal boundary conductance of Al/Si and Al/sapphire systems with Ni and Ta interlayers. Thermal boundary conductance in the absence of interlayers for Al/Si and Al/Sapphire was measured to be 250 $MWm^{-2}K^{-1}$ and 200 $MWm^{-2}K^{-1}$, respectively. The *G* value measured (G_{expt}) for Al/Si is in good agreement with previous reports ranging between 220 $MWm^{-2}K^{-1}$ – 300 $MWm^{-2}K^{-1}$ [6], [36], [59] [64]. Boundary conductance between Al/sapphire is slightly lower than reported values [40], [59]. This can be due to the presence of residual impurities on the surface of substrate. The *G* values predicted from the model (G_{model}) for Al/Si and Al/sapphire are ~245 $MWm^{-2}K^{-1}$ and ~235 $MWm^{-2}K^{-1}$, respectively, when considering all inelastic processes with acoustic phonon of sapphire, whereas the values increase to ~290 $MWm^{-2}K^{-1}$ and ~410 $MWm^{-2}K^{-1}$ after considering inelastic optical phonon contribution in Al/Si and Al/sapphire, respectively. The difference between G_{expt} and G_{model} shows that optical phonons in sapphire and silicon contribute very little to the total thermal boundary conductance.

4.3.1 Nickel Interlayer

Fig. 4.3 shows the evolution of *G* from experiment (G_{expt}) and thermal model (G_{model}) as a function of thickness in Al/sapphire system on addition of Ni interlayer. Experimental results are represented by filled circles. For the Al/Ni/sapphire, the saturated G_{expt} and G_{model} are ~ 165 $MWm^{-2}K^{-1}$ and ~ 210 $MWm^{-2}K^{-1}$ at 2 nm, respectively. As the Ni thickness increases, *G* has a local minimum around ~ 0.75 nm. The presence of the local minimum can be attributed to the similar vibrational properties of Ni and Al (Table 1) and higher electron-phonon coupling strength of Ni ($g = 1.05 \times 10^{18}\ Wm^{-3}K^{-1}$) with respect to Al ($g = 0.23 \times 10^{18}\ Wm^{-3}K^{-1}$).

Al/sapphire and Ni/sapphire have similar G_{pp} due to the similar vibrational properties of Al and Ni. Hence, at higher (Ni/sapphire) and lower (Al/sapphire) interlayer thicknesses G remains unchanged. At lower Ni thicknesses, *pathway 1* dominates over *pathway 2* because of two reasons:

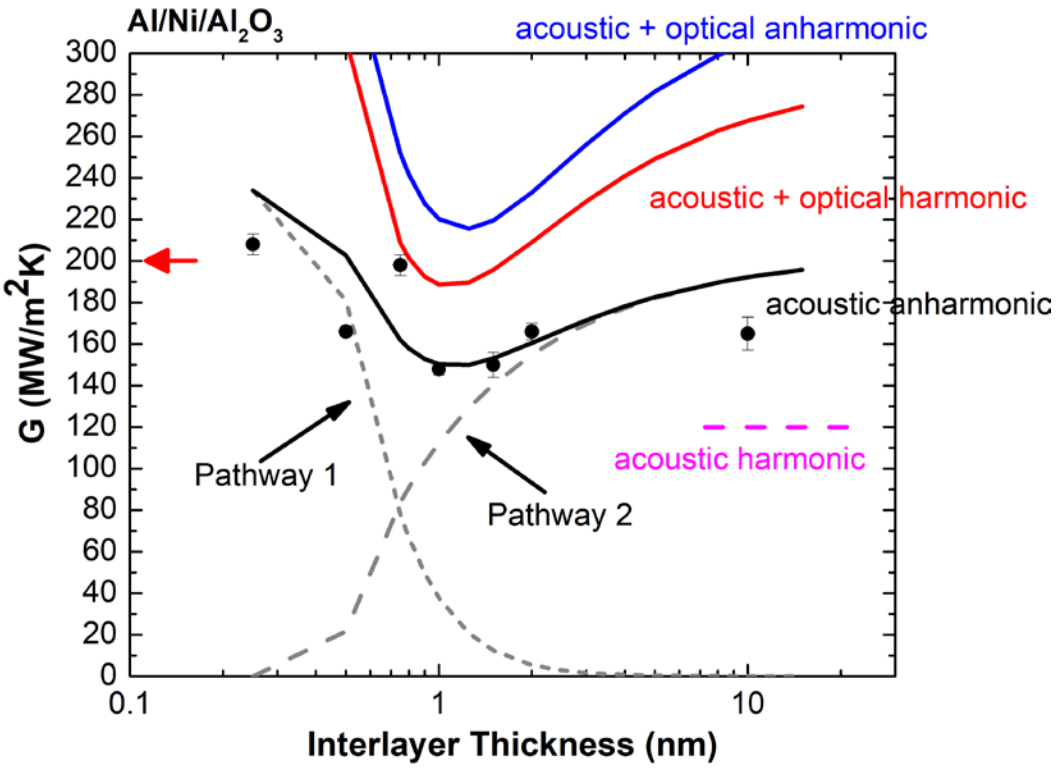

Fig. 4.3. Comparison of experimental G with the model as a function of interlayer thickness for the Al/Ni/sapphire system. Experimental results are represented by filled circles. The red arrow denotes the reference Al/sapphire boundary conductance. Dotted lines show the boundary conductance due to *pathway 1* and *pathway 2* as a function of interlayer thickness. The black solid curve represents the total G evolution (G_{model}) with increasing interlayer thickness considering all the anharmonic interactions with the acoustic phonons in sapphire. The red solid line denotes G_{model} considering elastic interactions of all the phonon modes in sapphire. The blue solid curve shows the inelastic interactions of all phonon modes in sapphire. Pink dashed line represents the G_{model} for Ni/sapphire considering elastic process with acoustic phonons in sapphire without considering the thickness–dependence of interlayer.

1) less phonon contribution from interlayer, 2) the resistance due to electron-phonon coupling in Ni is very high (negligible conductance). This high resistance acts in series with $G_{pp,2}$ reducing the overall conductance of *pathway 2*. As the Ni thickness increases, phonon contribution of interlayer increases and the resistance from coupling decreases due to high *g* for Ni; In this case, pathway 2 dominates pathway 1. Fig. 4.4 shows the evolution of G_{model} as a function of thickness without considering electron-phonon coupling effect in interlayer for Al-Ni-sapphire. The figure clearly shows that local minimum is more pronounced when electron-phonon coupling in the interlayer is considered. In the intermediate region, the local minimum happens at a thickness where the conductance due to electron-phonon coupling is high enough to act in series with the phonon-interlayer/phonon-substrate conductance to overrule the effect of direct phonon transmission from Al to substrate. This means that the high electron-phonon coupling of the interlayer (with respect to top metal layer) enhances the *pathway 2* conductance.

The overall evolution of *G* (G_{expt} and G_{model}) shows a local minimum and increases back to the saturated Ni/sapphire *G* value at higher interlayer thicknesses. Moreover, Fig. 4.4 shows that accounting for the electron-phonon coupling in interlayer makes the evolution of *G* with thickness slower, which is in good agreement with the experimentally observed *G*-evolution trend. Hence, at low interlayer thicknesses, electron-phonon coupling in the interlayer plays a significant role in determining the thermal boundary conductance evolution with thickness.

In order to check the validity of our experimental data, we performed DMM analysis assuming elastic and multiple-phonon inelastic scattering at the metal/dielectric interface. Fig. 4.3 represents the comparison of experimental *G* with the model as a function of interlayer thickness for Al/Ni/sapphire system. The red arrow denotes the reference Al/sapphire boundary conductance

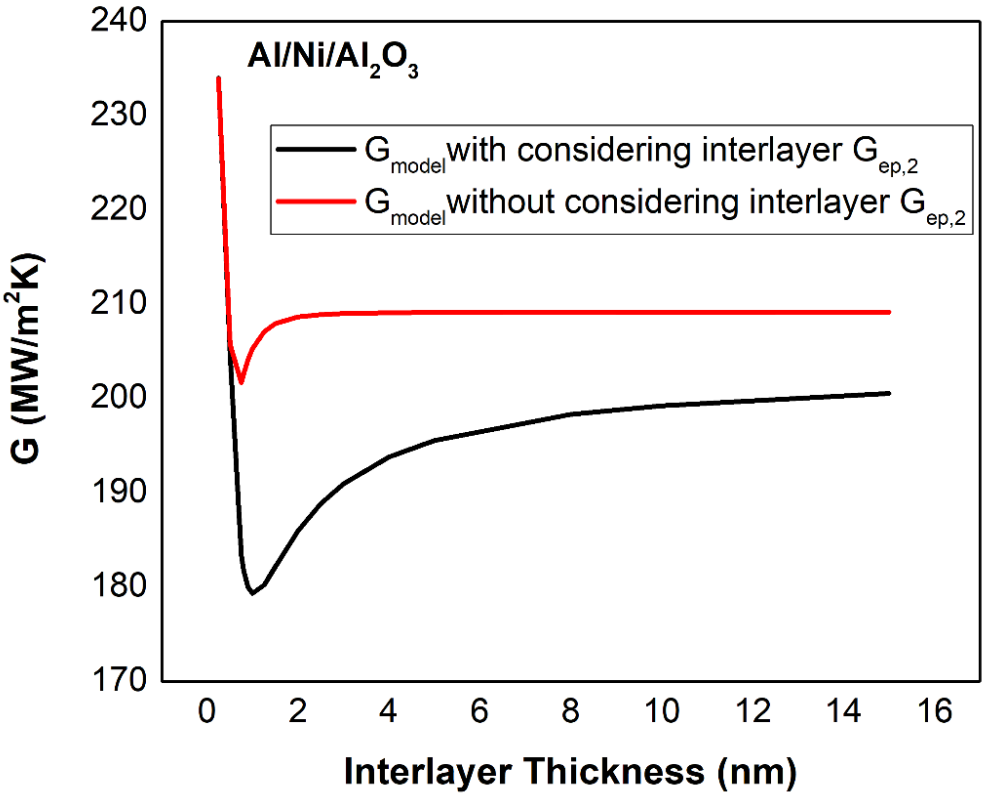

Fig. 4.4. Comparison of G_{model} with and without $G_{ep,2}$ in Al/Ni/sapphire system. The red curve represents the G_{model} without accounting for interlayer electron-phonon coupling. Black curve represents the interlayer electron-phonon coupling with accounting for interlayer electron-phonon coupling.

from experiments. Dotted lines show the boundary conductance due to *pathway 1* and *pathway 2* as a function of interlayer thickness. Black solid curve represents the total *G*-evolution (G_{total}) with increasing interlayer thickness considering all the anharmonic interactions with the acoustic phonons in sapphire. Red solid line denotes G_{model} considering elastic interactions of all the phonon modes in sapphire. Blue solid curve shows the inelastic interactions of all phonon modes in sapphire. Pink dashed line represents the G_{model} for Ni/sapphire considering elastic process with acoustic phonons in sapphire without considering thickness dependence of interlayer. For Al/Ni/sapphire system, the thermal boundary conductance predicted from model considering all

anharmonic scattering processes with the acoustic phonons in sapphire agrees well with the experiment. This is because only the low-energy phonons in sapphire are most likely to participate in the inelastic processes. Hence, accounting for all-optical phonons in the model overestimates the experimental results.

A similar trend was observed for Al/Si system on addition of Ni interlayer. Fig. 4.5 shows the thermal boundary conductance evolution with respect to thickness for Al/Ni/Si system. Experimental results are represented as black filled circles. The measured *G* value for Al/Ni/Si system reaches a saturation of about ~250 $MWm^{-2}K^{-1}$ at 2 nm. The thickness dependent *G* predicted from model for Al/Ni/Si system has a local minimum at ~1 nm, whereas experiment shows a local minimum at ~0.25 nm. This is because *G* accumulation in model starts only at Brillouin zone edge, and the interfacial effects before that thickness are not captured in the model. DMM modeling was done based on both elastic and inelastic phonon scattering between metal and dielectric. Fig. 4.5 also shows the comparison of experimental *G* with the model as a function of interlayer thickness for Al/Ni/Si system. The blue arrow denotes the reference Al/Si boundary conductance. Gray dotted and dashed lines represent the boundary conductance due to *pathway 1* and *pathway 2* as a function of interlayer thickness respectively. Black solid curve represents the total *G* evolution (G_{model}) with increasing interlayer thickness considering all the anharmonic interactions with the acoustic phonons in Si. Red solid line denotes G_{model} considering elastic interactions of all the phonon modes in Si. Blue solid curve shows the inelastic interactions of all phonon modes in Si. Pink dashed line represents the G_{model} for Ta/Si considering elastic process with acoustic phonons in Si without considering the thickness–dependence of interlayer. The model agrees reasonably well with the experimental *G* values and predicts the *G* evolution trend as a function of interlayer thickness.

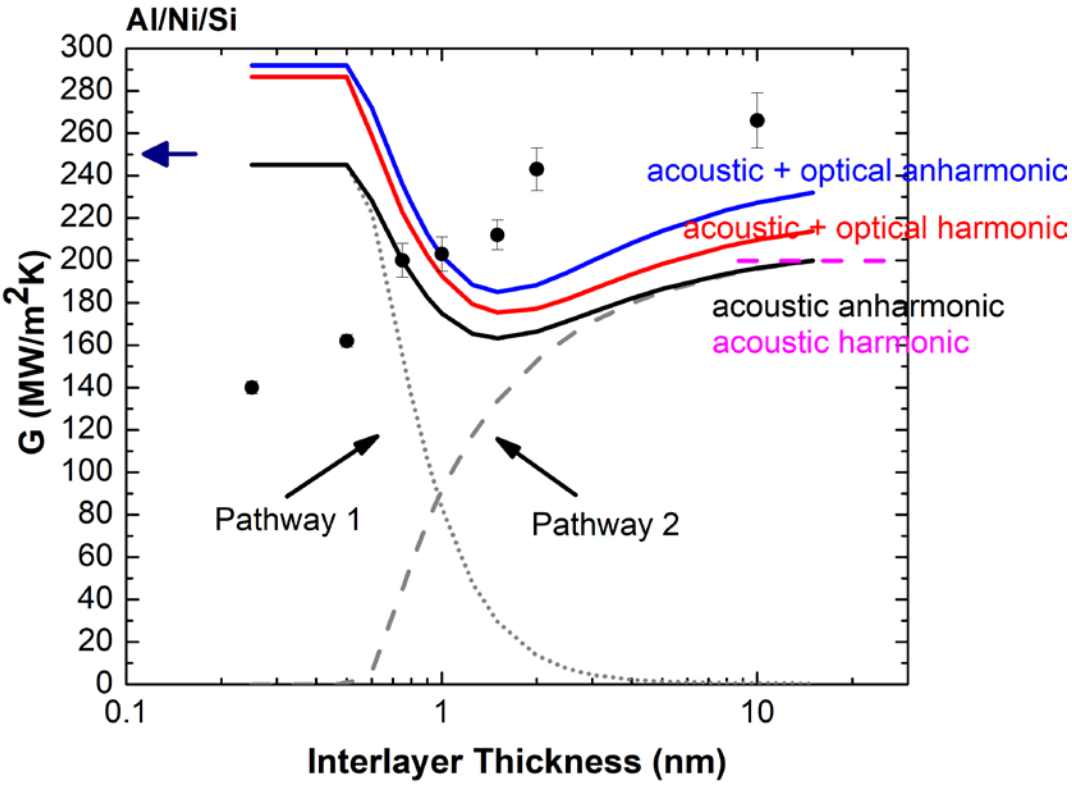

Fig. 4.5. Comparison of experimental *G* with the model as a function of interlayer thickness for Al/Ni/Si system. Experimental results are represented as filled circles. The blue arrow denotes the reference Al/Si boundary conductance. Gray dotted and dashed lines represent the boundary conductance due to *pathway 1* and *pathway 2* as a function of interlayer thickness respectively. Black solid curve represents the total *G* evolution (G_{model}) with increasing interlayer thickness considering all the anharmonic interactions with the acoustic phonons in Si. Red solid line denotes G_{model} considering elastic interactions of all the phonon modes in Si. Blue solid curve shows the inelastic interactions of all phonon modes in Si. Pink dashed line represents the G_{model} for Ni/Si considering elastic process with acoustic phonons in Si without considering the thickness–dependence of interlayer.

4.3.2 Tantalum Interlayer

When a Ta interlayer was inserted between Al/sapphire (Fig. 4.6) and Al/Si (Fig. 4.7), we observed a fast monotonic decrease in thermal boundary conductance with increasing thickness. The fast saturation (within 2 nm) in Al/Ta system can be attributed to the strong electron-phonon

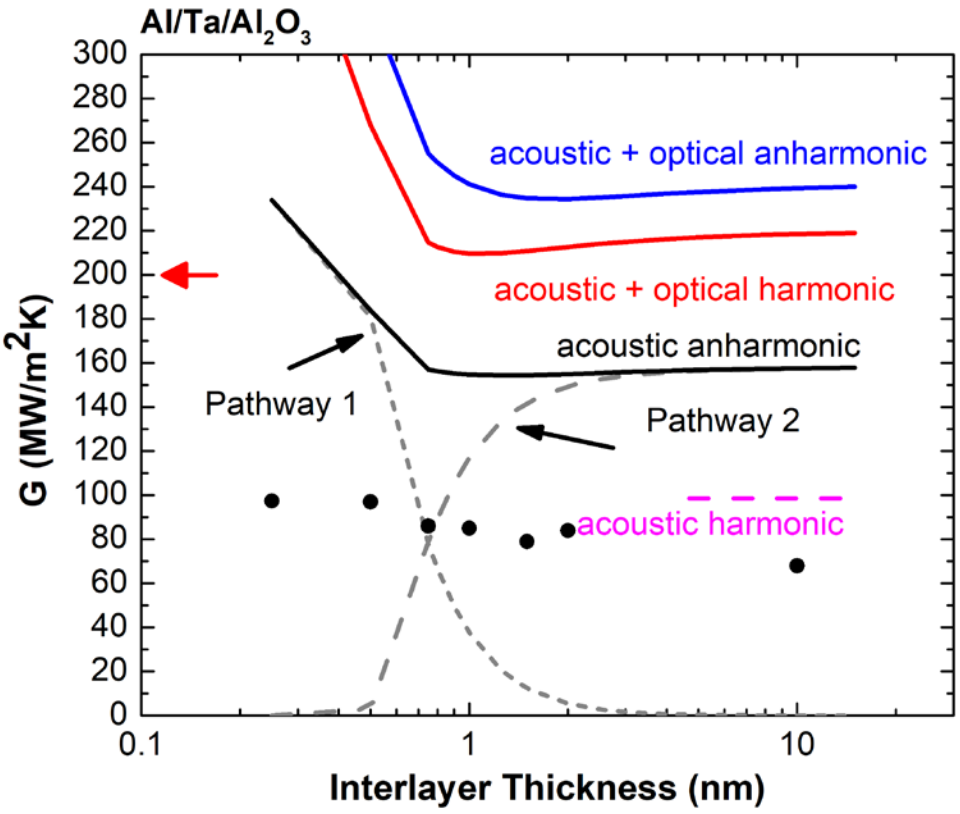

Fig. 4.6. Comparison of experimental *G* with model as a function of interlayer thickness for Al/Ta/sapphire system. Experimental results are represented by filled circles. The red arrow denotes the reference Al/sapphire boundary conductance. The gray dotted and dashed line represents the boundary conductance due to *pathway 1* and *pathway 2* as a function of interlayer thickness. Black solid curve represents the total *G* evolution (G_{model}) with increasing interlayer thickness considering all the anharmonic interactions with the acoustic phonons in sapphire. Red solid line and denotes G_{model} considering elastic interactions of all the phonon modes in sapphire. Blue solid curve shows the inelastic interactions of all phonon modes in sapphire. Pink dashed line represents the G_{model} for Ta/sapphire considering elastic process with acoustic phonons in sapphire without considering the thickness–dependence of interlayer.

coupling in Ta (g= 31 × 10^{18} $Wm^{-3}K^{-1}$). The strong g in Ta reduces resistance by readily dragging the system into equilibrium. Fig. 4.6 shows that relatively stronger g in Ta with respect to Ni induces a fast saturation of *G* as a function of interlayer thickness. Thus, we can conclude that as

the g strength increases, the thermal boundary conductance saturates faster as a function of thickness. The completely different vibrational properties of Ta and Al (Table 1) introduce a mismatch at the interface, hindering phonon transmission. Fig. 4.8 shows the phonon dispersion branch overlap between various metals Al, Ni, and Ta with sapphire and Si. We choose the directions based on metal film growth orientation on Si and sapphire. We choose $\Gamma \rightarrow X\ (100)$ direction in Al, $\Gamma \rightarrow L\ (111)$ in Ni, $\Gamma \rightarrow N\ (110)$ in Ta, $\Gamma \rightarrow Z\ (0001)$ in sapphire, and $\Gamma \rightarrow X\ (100)$ in Si. The plots clearly show that Ta has the worst overlap with Si and sapphire, which in turn reduces the phonon flux at the interface. This reduces the overall thermal boundary conductance for Al/Ta/Si and Al/Ta/sapphire systems (decreasing trend in *G*). For both Al/sapphire and Al/Si systems, the *G* value reached a plateau at 70 $MWm^{-2}K^{-1}$ once the thickness reached ~ 1 nm. For Al/Ta/sapphire system, *G* saturates at ~ 1 nm in both model and experiment, due to the strong electron-phonon coupling in Ta. Both experiment and model show a sharp decrease in thermal boundary conductance until it plateaus at ~ 1 nm. For Al/Ta/Si system, the experimental data saturates by ~ 1 nm but the model saturates ~ 2 nm (Fig. 4.7). This is because – as mentioned before – interfacial effects are not fully captured by model in both Al/Ni/Si and Al/Ta/Si systems due to the fact that accumulation starts only from Brillouin zone edge. For Ta interlayer, optical phonons in sapphire do not contribute to the overall *G* due to the large energy difference between highest acoustic phonon in Ta and lowest optical phonon in sapphire. The reduction in phonon flux at the interfaces reduces the overall *G*. In both Al/Ta/sapphire and Al/Ta/Si, DMM overpredicts the Ta/sapphire and Ta/Si *G* values. This can be due to three reasons: 1) acoustic phonons in Si and sapphire are higher in energy compared to Ta acoustic phonons, which reduces the phonon flux at the interface; 2) we considered all anharmonic processes in Ta/Sapphire and Ta/Si system. Because of the large energy difference between Ta and substrates

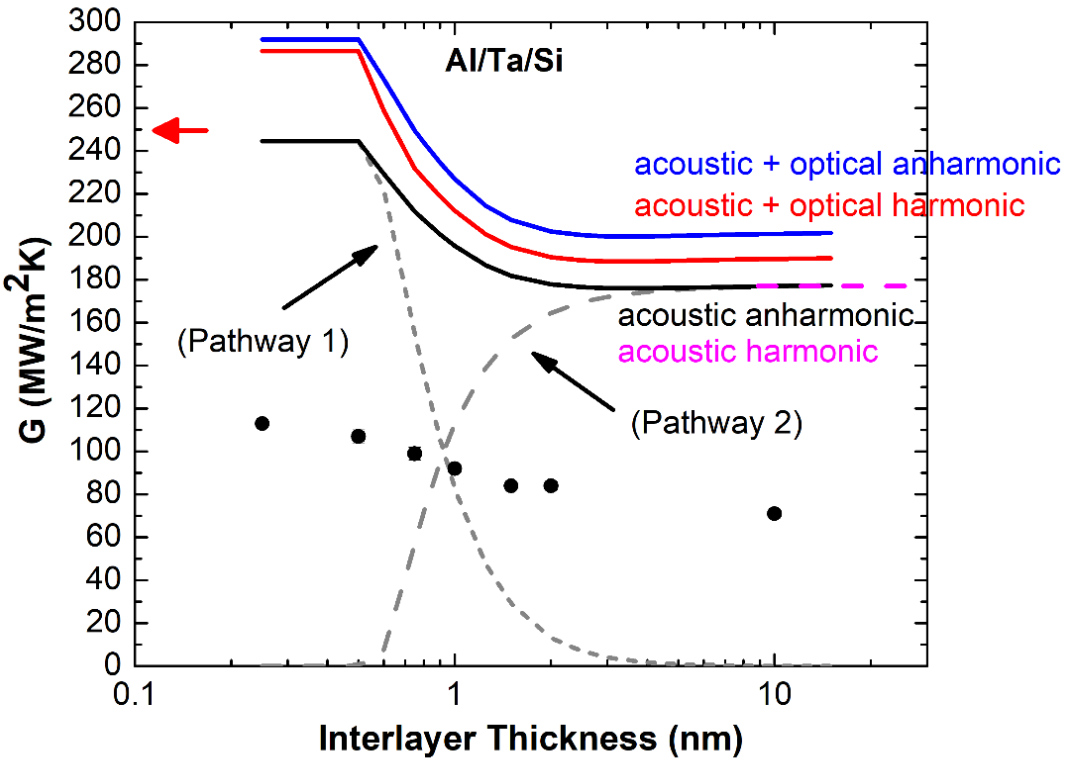

Fig. 4.7. Comparison of experimental *G* with the model as a function of interlayer thickness for Al/Ta/Si system. Experimental results are represented as filled circles. The blue arrow denotes the reference Al/Si boundary conductance. The green dotted line and grey dashed line represents the boundary conductance due to *pathway 1* and *pathway 2* as a function of interlayer thickness. The black solid curve represents the total *G* evolution (G_{model}) with increasing interlayer thickness considering all the anharmonic interactions with the acoustic phonons in Si. Red solid line and denotes G_{model} considering elastic interactions of all the phonon modes in Si. Blue solid curve shows the inelastic interactions of all phonon modes in Si. Pink dashed line represents the G_{model} for Ta/Si considering elastic process with acoustic phonons in Si.

(Si and sapphire) the probability for higher-order inelastic process decreases. The probability for higher-order anharmonic processes always decreases with increasing number of participating phonons; 3) inaccurate phonon dispersions for calculating thermal boundary conductance and phonon transmission coefficient. The phonon dispersion used for *G*-calculation strongly depends on the choice of crystal orientation. We chose directions based on metal film growth orientation

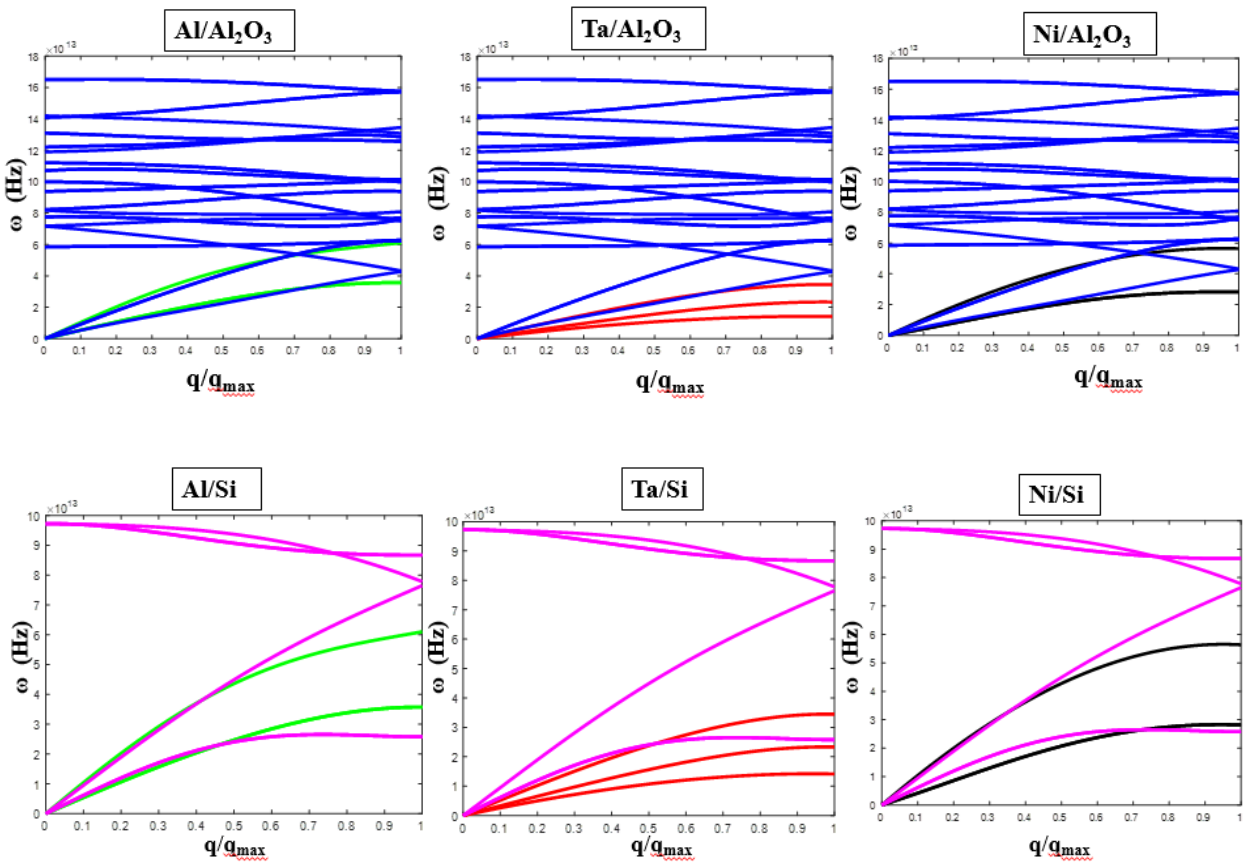

Fig. 4.8. Phonon dispersion of metals and dielectric materials used in this work. Blue and pink curves represent the phonon dispersion branches for sapphire and Si, respectively. Green, red, and black represents the Al, Ta, and Ni phonon dispersion branches, respectively.

(110 for Ta) on Si and sapphire. However, Tantalum has shown to grow in both 110 and 111 orientation in (0001) sapphire [65]. Hence, an inaccurate selection of phonon dispersion can affect G-calculation. The model captures the experimental *G* trend reasonably well and thus can be used as a tool for predicting the evolution of thermal boundary conductance as a function of thickness.

We used the above-mentioned formulation to predict the *G* evolution for the data published by Jeong et al [13]. Fig. 4.9 shows the comparison of model and data from Ref. [13] with our model for Au/Cr/sapphire system. Au and sapphire have completely different vibrational

properties like Ta and sapphire. Inserting a Cr interlayer enhances the *G* by increasing the phonon availability at the interface. Au has a much weaker electron-phonon coupling comparing to Cr. However, Cr has a weaker *g* than Ni and Ta, thus the comparatively weaker *g* in Cr induces a slower saturation (saturates by ~5 nm) in *G* with respect to thickness.

The plot clearly suggests that electron-phonon coupling in the interlayer should not be neglected and when weak it causes a slower saturation in the thickness dependence boundary conductance.

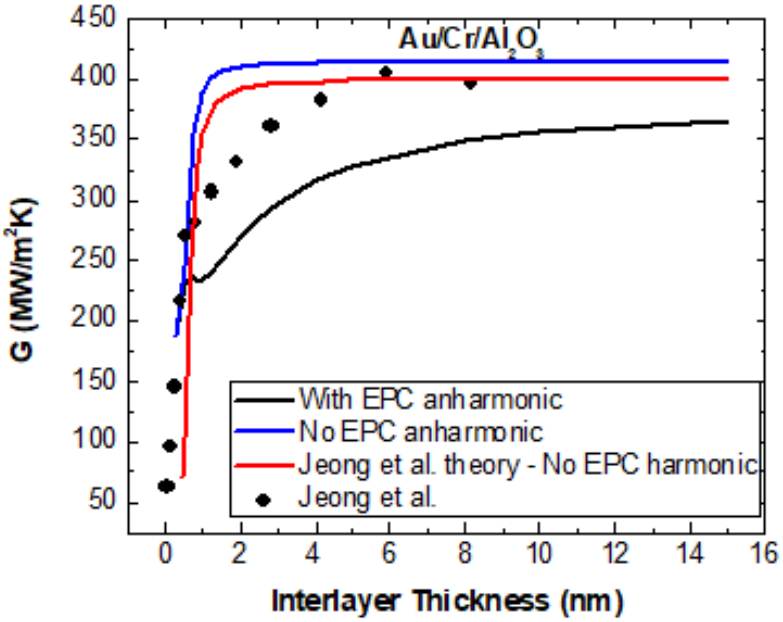

Fig. 4.9. Comparison of our model with the results published in Ref. [13]

4.4 Conclusion

In summary, we studied the thickness dependence of an interlayer at a metal-dielectric boundary. We suggest that very thin interface layers can alter the *G* at metal/dielectric interfaces

considerably. The thickness dependent thermal boundary conductance in Al/Si and Al/sapphire changes significantly within the initial few nanometers and reaches saturation before ~5 nm on addition of Ni and Ta interlayers. When the interlayer has a strong electron-phonon coupling constant, the evolution of G is fast and happens within 2 nm. When g is weak, thermal boundary conductance saturates slowly. Thus, the electron-phonon coupling of the interlayer plays a major role in determining the trend of G evolution with thickness.

CHAPTER 5

MECHANISMS OF THERMAL TRANSPORT AT METAL-DIELECTRIC INTERFACES ON ADDITION OF ULTRATHIN INTERLAYERS

As mentioned in Chapter 1, tuning the thermal boundary conductance at metal-dielectric interfaces require the knowledge of various interfacial properties. In the previous chapter, we established that the contribution of electron-phonon coupling in the interlayer must be taken into account for the calculation of total interfacial thermal conductance. We also found that on addition of Ni and Ta interlayers, the thermal boundary conductance saturates before ~ 5 nm and the saturation thickness depends on interlayer electron-phonon coupling strength. This means a very thin interlayer is enough to modify (enhance or reduce) the total interfacial conductance.

In this chapter, we study the influence of a 5 nm thick metal interlayer at metal-dielectric interfaces. The primary purpose of this work is to systematically analyze various properties of interlayer and its effect on heat transport mechanisms at metal-dielectric interfaces. Besides the quality of interface (interface roughness, grain boundaries, interfacial defects) and adhesion strength, which are hard to measure and control systematically, vibrational properties and electron-phonon coupling of the interlayer are two major contributors to the total interfacial conductance (see section 1.1.3). In order to understand the contribution from vibrational properties, we look at the Debye temperature overlap and the acoustic phonon cut-off frequency mismatch between metal and substrate. We show that addition of interlayers with intermediate Debye temperature at

Al/sapphire and Al/quartz interfaces enhance the thermal boundary conductance due to the enhanced phonon flux at the interface. We also show that despite the similar Debye temperatures of sapphire (1047 K) and AlN (1150K), insertion of Ni and Cr interlayers between Au/sapphire and Au/AlN shows a striking difference in thermal boundary conductance at both the interfaces. The thermal boundary conductance measured for Au/interlayer/sapphire system, which has a better phonon cut-off frequency overlap, is ~70% higher than the *G* measured for Au/interlayer/AlN system with weak cut-off frequency overlap. Along with the vibrational properties, another factor that determines the interfacial thermal transport on addition of an interlayer is the electron-phonon coupling effect. Interlayers with strong *g* reduce the effective thermal resistance by reducing the non-equilibrium between electrons and phonons (see section 1.1.3). In order to verify the effects of electron-phonon coupling, we deposit a series of interlayers between Au/sapphire. We suggest that depending on the strength of coupling, electron-phonon interaction in the metal and interlayer can significantly alter the heat transport pathways in a metal-dielectric system.

5.1 Introduction

Modification of heat transport at solid-solid interfaces are increasingly important in heat management applications [12], [20]. As mentioned before, along with interface quality, electron-electron interaction, electron-phonon interaction, and phonon-phonon interaction are various mechanisms to transport heat in a metal-dielectric system. Previous works have shown that the insertion of a metallic interlayer can significantly alter the interfacial conductance at a metal-dielectric interface [13], [14], [25]. However, various mechanisms involved in thermal transport at the interface on addition of an interlayer is not well understood. Hence, the proper choice of an

interlayer to tune (enhance/reduce) thermal boundary conductance is still unknown. Analysis of the heat transport mechanisms in the presence of an interlayer at metal-dielectric interface requires the understanding of various factors that contribute to heat transfer. This work focuses on studying the heat transfer pathways at metal-dielectric interfaces on addition of ultrathin metallic interlayers, by systematically analyzing various interlayer factors that can contribute to interfacial thermal transport. As mentioned in section 1.1.3, the key parameters that determine the interfacial heat transport in a metal-dielectric system are phonon spectra and electron-phonon coupling of the metallic layer. Hence, this study is performed based on three interlayer parameters, specifically: Debye temperature (θ_D), acoustic phonon cut-off frequencies (v_T and v_L), and volumetric electron-phonon coupling (g).

We predicted that the addition of an interlayer with intermediate θ_D, v, and g at the metal-dielectric interface enhances the overall G because of the following reasons: Insertion of interlayers with intermediate θ_D should increase the total G because of the increased phonon density of states, which in turn enhances the phonon flux at the interface. Acoustic phonon cut-off frequencies in a metal determine the highest frequency phonon in the system. As mentioned before, highest frequency phonons in a material have the maximum phonon states and the availability of phonons at the interface can enhance the G due to increase in phonon flux. Hence, inserting a metallic interlayer with intermediate cut-off frequency should increase the G. Electron-phonon coupling constant g determines the energy exchange between electrons and phonons in a metal. The non-equilibrium between electrons and phonons is strong if the top metal layer has a weak g. This enhances the resistance channel for heat transport, which can reduce the overall G. Adding an interlayer with intermediate g at metal-dielectric interface should decrease the non-equilibrium by immediately dragging electrons and phonons into equilibrium. In order to verify our hypothesis,

we made a matrix of metal-interlayer-dielectric systems as shown in Table 2. The first column represents the interlayer parameters being tested. Second column represents the choice of metal

Table 2: Metal-Interlayer-Dielectric sample sets analyzing in this work

Interlayer Parameter	Metal-X- Dielectric (X- interlayer)	Choice of Interlayer	
Debye temperature (θ_D)	Al-X-Sapphire Al-X-Quartz	Al-**Ni**- Sapphire Al-**Cr**- Sapphire	Al-**Ni**-Quartz Al-**Cr**- Quartz
Volumetric electron-phonon coupling constant (g)	Au-X-Sapphire	Au-**Al**- Sapphire Au-**Ni**- Sapphire Au-**Cr**- Sapphire	
Acoustic phonon cut-off frequencies (ν_T and ν_L)	Au-X-AlN Au-X-Sapphire	Au-**Cr**-AlN Au-**Ni**-AlN	Au-**Cr**- Sapphire Au-**Ni**- Sapphire

and dielectrics for this study. The third column represents the choice of interlayer to insert in between metal and dielectric. The various thermophysical properties of metals and interlayers used in this study are given in Table 3. For understanding the role of θ_D (first row in Table 2), Al/sapphire and Al/quartz were chosen. Both sapphire and quartz have higher θ_D than Al (Table

3). Hence, adding an interlayer with intermediate Debye temperature should enhance the *G*. However, the Debye temperature of sapphire is twice than that of quartz. Thus, the magnitude of *G* in both systems will be different. The interlayers chosen for this analysis were Ni and Cr. Ni has similar θ_D to that of Al, whereas Cr has a much higher θ_D than both Al and Ni (Table 3).

Table 3: Thermophysical properties of different materials of interest in this work

Layer 1 Metals	Interlayer	Substrate
Au (Gold) θ_D =165K ν_L=5THz ν_T=1.8THz g=0.023×10^{18} W/(m^3 ·K)	Cr (Chromium) θ_D =630K ν_L= 9.6THz ν_T=7.7THz, 6THz g= 0.42×10^{18} W/(m^3 ·K)	α-Al_2O_3 θ_D =1047K ν_L=10THz ν_T= 6.9THz $\nu_{optical}$=26THz
Al (Aluminum) θ_D =428K ν_L=9.6THz ν_T=5.7THz g= 0.24×10^{18}W/(m^3 ·K)	Ni (Nickel) θ_D =450K ν_L = 9.1THz ν_T= 4.5THz g= 1.05×10^{18} W/(m^3 ·K)	Quartz θ_D =470K ν_L=4Thz ν_T=1.8THz $\nu_{optical}$=37THz
		AlN θ_D =1150K ν_L=17.6THz ν_T=10.3THz $\nu_{optical}$=27THz

Therefore, the expected trend in G for this set is,

$$G_{Al/sapphire} \approx G_{Ni/sapphire} < G_{Cr/sapphire} \qquad \text{(Prediction 1)}$$

$$G_{Al/quartz} \approx G_{Ni/quartz} > G_{Cr/quartz} \qquad \text{(Prediction 2)}$$

Cr has a higher θ_D than quartz and Al; hence, adding a Cr interlayer introduces phonon mismatch. In addition, since Al and quartz have similar θ_D this system has less phonon mismatch. Hence,

$$G_{Al/quartz} > G_{Al/sapphire} \qquad \text{(Prediction 3)}$$

To study the effect of acoustic phonon cut-off frequency (third row in Table 2), we study two set of samples: Au/AlN and Au/sapphire sample sets. Au has a large acoustic phonon cut-off frequency mismatch with respect to AlN and sapphire (Table 3.). Despite the similar θ_D for AlN and sapphire, they differ in the cut-off frequencies. Sapphire frequencies have better match with Au frequencies than AlN. Inserting Ni and Cr (intermediate cut-off frequency) should enhance the phonon transmission by increasing the availability of high-frequency phonons. Hence, the expected trend is,

$$G_{Au/sapphire} < G_{Ni/sapphire} < G_{Cr/sapphire} \qquad \text{(Prediction 4)}$$

$$G_{Au/AlN} < G_{Ni/AlN} < G_{Cr/AlN} \qquad \text{(Prediction 5)}$$

Since, sapphire phonons have better overlap with Au, Cr and Ni phonons,

$$G_{Au/sapphire} > G_{Au/AlN}$$

$$G_{Ni/sapphire} > G_{Ni/AlN} \qquad \text{(Prediction 6)}$$

$$G_{Cr/sapphire} > G_{Cr/AlN}$$

To verify the role of g, we select Au as the top metal layer, due to its relatively lower g compared to other common metals. The dielectric was sapphire. Inserting Al, Cr, and Ni with higher g than Au should enhance the G by reducing the resistance due to electron-phonon non-equilibrium. Hence the expected trend is,

$$G_{Au/sapphire} < G_{Al/sapphire} < G_{Cr/sapphire} < G_{Ni/sapphire} \qquad \text{(Prediction 7)}$$

In order to analyze the overall *G* in a metal-dielectric system, we developed a thermal model, which is explained in section 4.1. The various energy relaxation mechanisms at a metal-dielectric interface in the presence of an interlayer is shown in Fig. 4.1. As explained in section 4.1, the total interfacial conductance at a metal-interlayer-dielectric system involves two parallel heat transfer pathways. *Pathway 1* can be determined using Eq. 38. If the phonon wavelength is higher than interlayer thickness, they will directly pass to the dielectric. As the thickness of the interlayer increases, long wavelength phonon contribution decreases which in turn reduces the phonon flux at the interface and the *pathway 1* becomes negligible. Hence, based on the previously mentioned conditions for *pathway 1* to be negligible, in the presence of a 5 nm thick interlayer the Al-interlayer-substrate systems have a negligible contribution to *pathway 1* due to its strong *g*. On the other hand, for Au-interlayer-substrate systems, with a 5 nm thick interlayer, the contribution from $G_{pp,1}$ is small but the weak *g* in Au enhances the resistance of the system due to non-equilibrium between electrons and phonons. Hence, *pathway 1* is not negligible in Au-interlayer-dielectric systems.

In *pathway 2*, electrons in metal interact with the electrons in the metallic interlayer (G_{ee}), and subsequently, these electron transfers the energy to the cold lattice. The volumetric energy exchange between electrons and phonons can be represented by $G_{ep,2}$ and can be expressed using Eq. 41 or 38, depending on the interlayer thickness. Heat from the interlayer can then transfer to dielectric ($G_{pp,2}$) or can propagate back to the top metal (G_b) (see section 4.1.1). We suggest that heat can transfer back to the metal depending on the following two necessary conditions:

1) The *g* for top metal should be weak and the interlayer should have a higher *g* than top metal layer.

If the top metal layer has a strong *g* value, similar to or slightly less than interlayer, the back propagation will not happen (e.g. Al (Fig. 4.2)). On the other hand, for a metal with relatively low g value with respect to other common metals, such as Au ($g = 0.023\times10^{18}$ W/(m^3 ·K)) the back transfer effect should be more pronounced. In order to verify this hypothesis, we did a two-temperature model analysis for Au/Al and Au/Cr samples. Fig. 5.1 and 5.2 show the lattice temperature and electron temperature evolution as a function of time delay and layer thicknesses in bimetallic structures. The Au layer used in this model is 50 nm thick and the interlayers are 5 nm thick. The plots clearly show that due to the very low *g* in Au, the electron-phonon non-equilibrium in Au is very high which results in slow (or no) rise in Au lattice temperature. Since the interlayers (Cr and Al) has a much stronger *g* than Au, the temperature of interlayer lattice increases more quickly than Au due to fast equilibration of electrons and phonons in interlayer. This will result in a backflow of heat from interlayers to Au. Fig. 5.3 shows the schematic temperature profiles for electrons (T_e) and phonons (T_i) across a metal-interlayer-dielectric system when Al is the top metal layer. Here, we assume that the interlayers have higher *g* than Al (same as experiment condition). The red curve represents the electron temperature evolution and blue curve represents the phonon temperature. Since the *g* in Al is very high, electrons and phonons equilibrate fast enough and, hence, no phonon back transfer takes place. The interlayer has higher *g* than Al and, hence, equilibrates much faster than Al. Fig. 5.4 represents the electron and phonon temperature profiles in a metal-interlayer-dielectric system when Au is the top metal layer. The interlayer has a *g* much greater than Au (same as experiment condition). The weak *g* in Au causes a strong non-equilibrium between electrons and phonons and adding an interlayer with stronger *g* in between reduces the non-equilibrium, which promotes back transfer of heat. Hence, two-temperature model verified the hypothesis.

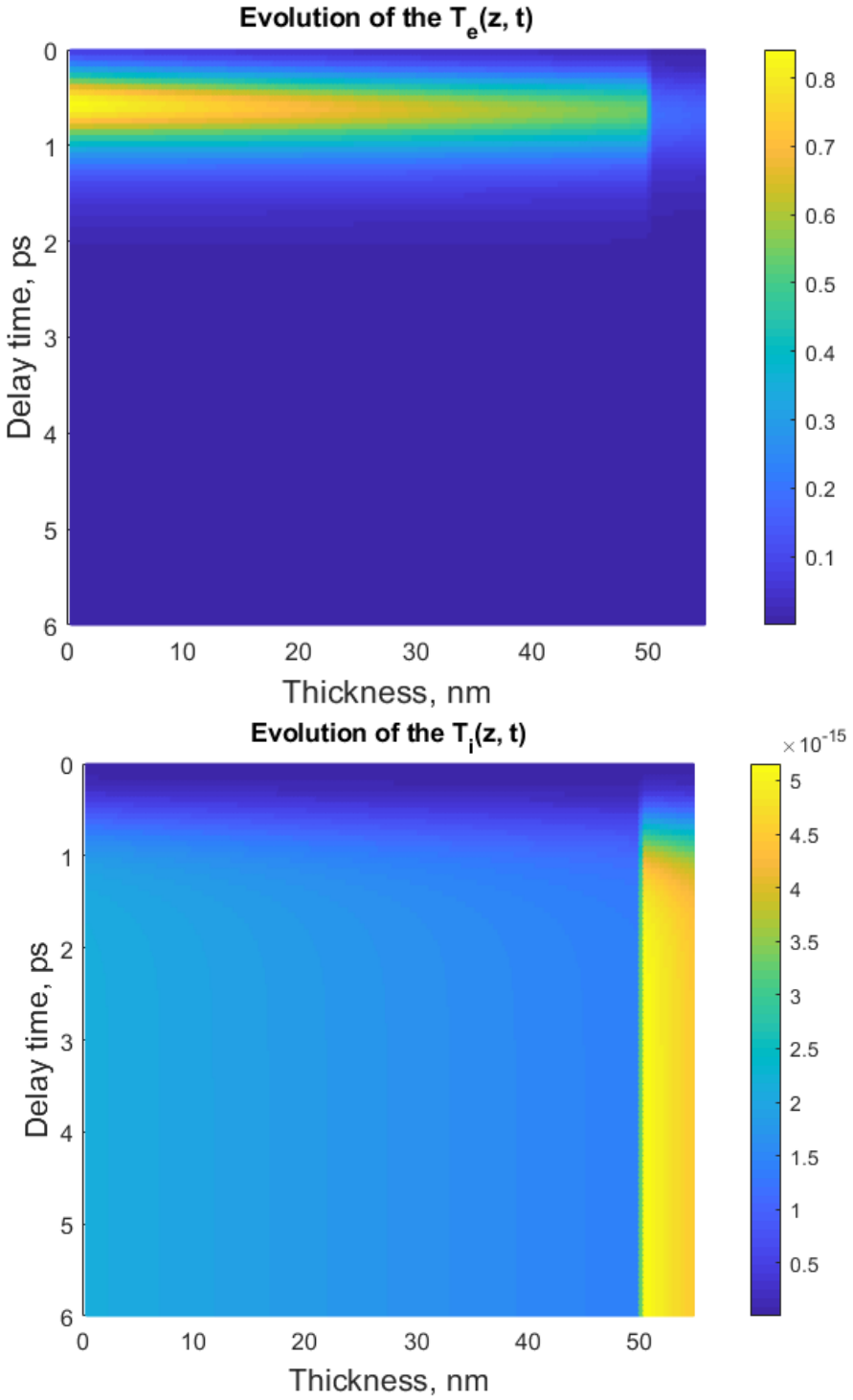

Fig. 5.1. The electronic ($T_e(z,t)$) and lattice temperature ($T_i(z,t)$) evolution as a function of delay time and bimetallic layer thickness in Au (50 nm)-Al (5 nm) system. The 50 nm marks the interface between Au and Al. The plot shows that due to relatively low g in Au the electron and phonon temperature difference is high and since the Al layer has a higher g, the electrons and phonons equilibrate faster, raising the Al lattice temperature. This leads to backflow of heat from Al to Au.

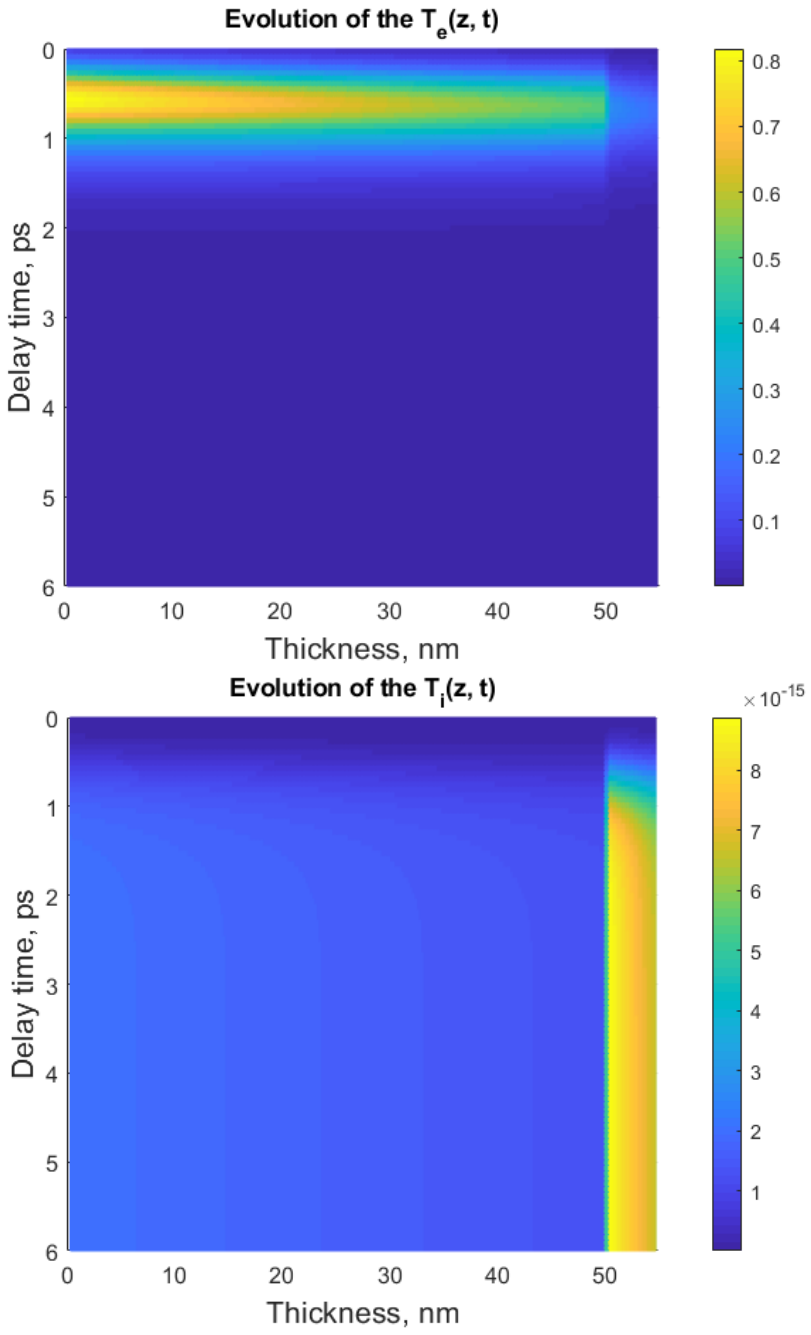

Fig. 5.2. The electronic ($T_e(z,t)$) and lattice temperature ($T_i(z,t)$) evolution as a function of delay time and bimetallic layer thickness in Au (50 nm)-Cr (5 nm) system. The 50 nm marks the interface between Au and Cr. The plot shows that due to relatively low g in Au the electron and phonon temperature difference is high and since the Cr layer has a higher g, the electrons and phonons equilibrate faster, raising the Cr lattice temperature. This leads to backflow of heat from Cr to Au.

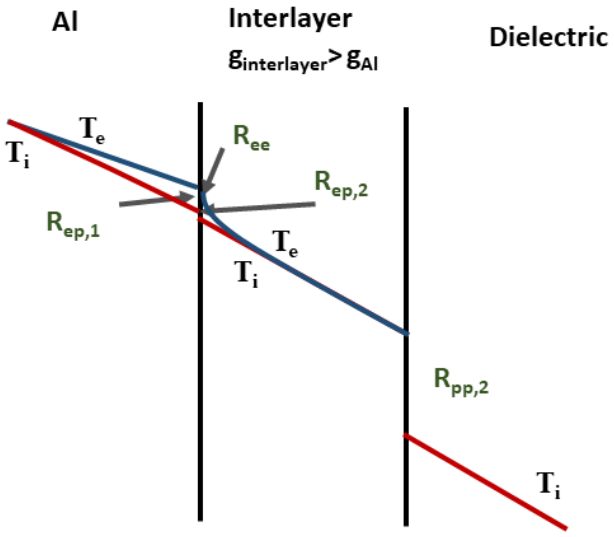

Fig. 5.3. Schematic temperature profiles for electrons (T_e) and phonons (T_i) across a metal-interlayer-dielectric system when Al is the top metal layer. Here we assume that interlayer has a g higher than Al.

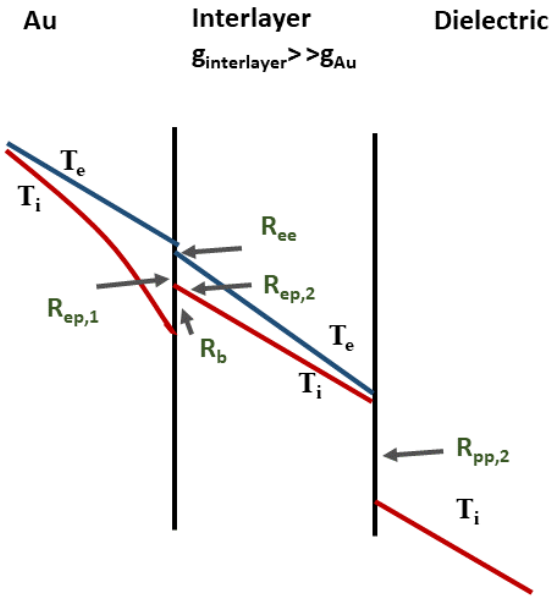

Fig. 5.4. Schematic temperature profiles for electrons (T_e) and phonons (T_i) across a metal-interlayer-dielectric system when Au is the top metal layer. Here we assume that interlayer has a g much higher than Au.

2) The time constant ($\tau_{interface} = hc_p/G$) for the interlayer-dielectric heat transfer should be higher than that of interlayer-metal time constant.

As mentioned in the previous chapter, this condition is necessary to ensure that the direction of heat propagation is back to the metal and not to the dielectric. This condition is always valid in our experiments because, the resistance pathway due to phonon-interlayer/phonon-dielectric has a smaller *G* (or higher $R_{pp,2}$) in comparison with phonon-interlayer/phonon-top metal interaction. It should be noted that the above-mentioned two conditions are necessary for back transfer to happen.

The thermal boundary conductance at a metal-interlayer-dielectric system can be modeled assuming the resistance due to *pathway 1* and *pathway 2* are in parallel using Eq. 41. The current thermal model for analyzing metal-interlayer-dielectric systems does not account for the resistance due to backpropagation.

5.3 Results and analysis

5.3.1 Thickness dependence of interlayer

From the previous chapter, we established that the thickness-dependent thermal boundary conductance at a metal-dielectric interface reaches saturation before ~5 nm if the interlayers have relatively strong electron-phonon coupling constant. We also said that for Al-interlayer-dielectric system, the contribution from $G_{ep,1}$ is negligible due to the strong *g* for Al. However, for Au, since the Au *g* is weak, large resistance due to electron-phonon coupling must be taken into account in the thermal model. To verify this, we did a thickness-dependent study in Au/Ni/sapphire to understand the contribution of electron-phonon coupling in Au. We inserted ultrathin layers (0.5

nm-5 nm) of Ni between Au/sapphire and measured the thermal boundary conductance of those samples. Details of the thickness dependence study can be found in Chapter 4.

Pathway 1 can be calculated from Eq. 38 and the contribution from $G_{ep,1}$ in top metal layer was calculated from Eq. 38. The total thermal boundary conductance from thermal model (G_{model}) was calculated using Eq. 42. In Fig. 5.5, red circles represent the experimentally (G_{expt}) measured G in Au/Ni/sapphire system and the green arrow represents the reference G in Au/sapphire. Black solid curve shows the G from the model (G_{model}), which ignores the electron-phonon coupling in Au layer ($G_{ep,1}$). Blue solid curve shows the G from model (G_{model}), which accounts for the

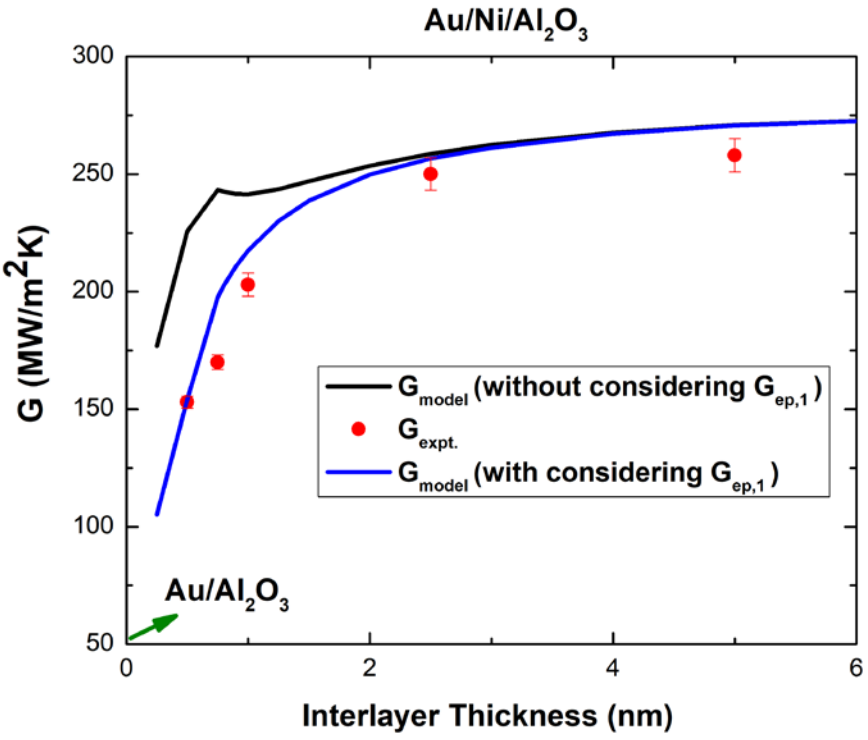

Fig. 5.5. Thickness dependence of Au/Ni/sapphire system. Red circles represent the experimentally measured G and the green arrow represents the reference G_{expt} for Au/sapphire. Black solid curve shows the G from the model (G_{model}), which ignores the electron-phonon coupling in Au layer ($G_{ep,1}$). Blue solid curve shows the modeled G (G_{model}), which accounts for the electron-phonon coupling in Au layer.

electron-phonon coupling in Au layer. The plots clearly show that when there is a strong non-equilibrium in the top metal layer, resistance due to the non-equilibrium also must be taken into account. In addition to this, as established from previous chapter, when Ni is added as an interlayer, thermal boundary conductance saturates by ~ 2 nm. The interlayer thickness in our metal-dielectric system is fixed at 5 nm because for all the interlayers in this study the *G* is strong enough to saturate before 5 nm.

5.3.2 Role of Debye temperature

As mentioned before, to understand the role of Debye temperature, we analyze two systems: Al/interlayer/sapphire and Al/interlayer/quartz. Thermal boundary conductance for Al/sapphire system was measured to 200 $MWm^{-2}K^{-1}$. This is slightly lower than the reported values [40], [59]. This can be due to the presence of residual impurities on the substrate surface. When a 5 nm Ni interlayer was inserted between Al/sapphire, the measured *G* value was ~ 240 $MWm^{-2}K^{-1}$. Overall thermal conductance of Al/Ni/sapphire and Al/sapphire similar due to the similar Debye temperature of Ni and Al (Table 3). However, addition of a Cr layer at the Al/sapphire boundary enhanced the thermal boundary conductance to ~ 320 $MWm^{-2}K^{-1}$. Comparing with Al, Cr has a higher Debye temperature – or has better phonon DOS overlap with sapphire (Fig. 5.6). As evident from Fig. 5.6, high-frequency phonons have the highest density of states and the highest number of phonon contributions being from Cr and sapphire. Thus, the contribution to interfacial phonon flux is highest for Cr among Ni and Al. As expected, Al/Cr/sapphire sample shows the highest *G* measured. The data clearly shows that adding a material with intermediate Debye temperature can increase the *G*. Thus, Prediction 1 is verified.

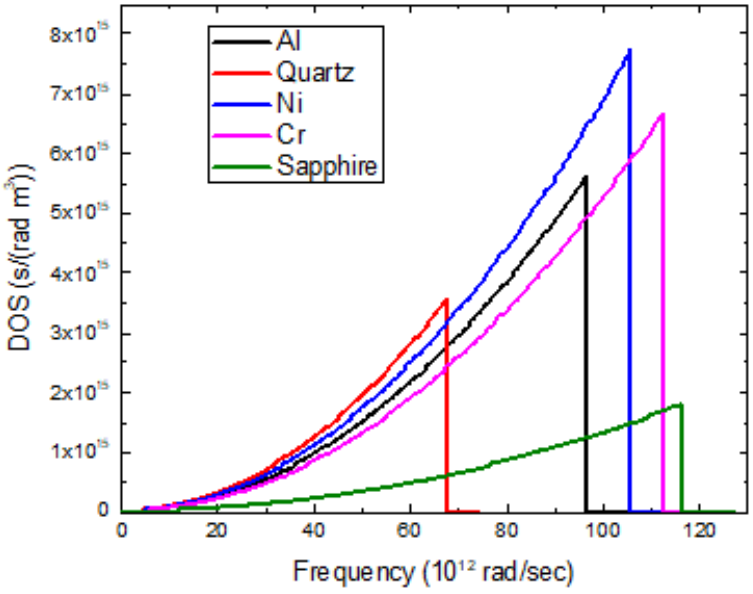

Fig.5.6. Debye phonon DOS for Al, Ni, Cr, Quartz and Sapphire

For the quartz substrate, measured Al/quartz thermal boundary conductance was ~165MWm^{-2}K^{-1}. Addition of Ni and Cr interlayers altered the thermal boundary conductance slightly, to ~180 MWm^{-2}K^{-1} and ~150 MWm^{-2}K^{-1} respectively. The *G*-values for Al/quartz, Al/Ni/quartz, and Al/Cr/quartz are very similar, and thus the analysis to compare with our prediction is difficult. However, with the above-measured value for *G*, Al/Cr/quartz has the lowest *G* as expected from the trend. On the other hand, Al/Ni/quartz shows the highest *G* followed by Al/quartz. Ni has a slightly higher Debye temperature than Al and as evident from the Fig. 5.6, the quartz phonons at higher frequencies has a better overlap with Ni followed by Al and Cr. Thus, the phonon flux at the interface is highest for Al/Ni/quartz system. Hence, as expected, adding a material with intermediate Debye temperature can enhance the thermal boundary conductance (Prediction 2 verified).

To analyze the third prediction, we compare the G values for Al/sapphire and Al/quartz. The experimentally observed values are 200 $MWm^{-2}K^{-1}$ and 165 $MWm^{-2}K^{-1}$. The experiments clearly show that $G_{Al/sapphire} > G_{Al/quartz}$. This observation contradicts the prediction because Al and quartz have similar Debye temperatures and, hence, should have a better G than Al/sapphire.

Analyzing the data further shows that, the similarity in the experimentally measured G for Al/quartz, Al/Ni/quartz, and Al/Cr/quartz can be explained in terms of acoustic cut off frequencies. Due to the large Debye temperature difference between Cr and quartz, ideally Cr should show a much lower G than what we measured. The similarity in G is due to the relatively alike phonon frequencies of all Al, Ni, and Cr metals with respect to quartz (Table 3). The longitudinal acoustic cut-off frequencies (v_L) for Al, Ni, and Cr are at ~9.6 THz, ~9.1 THz and ~9.6 THz , whereas for quartz, v_L is ~ 4 Thz. Hence, the contribution to phonon flux at the interface is small and similar for all Al/quartz, Al/Ni/quartz, and Al/Cr/quartz. Further, the transverse acoustic phonon cut-off frequencies for Al, Ni, Cr and quartz are 5.7 Thz, 4.5 THz, ~7THz and 1.8 Thz. The low-frequency acoustic phonons in quartz have better overlap with Ni, which in turn enhances the boundary conductance in Al/Ni/quartz system. The discrepancy in Prediction 3 can also be explained from the above concept. Al (v_L =9.6 THz, v_T =5.7 THz) and sapphire (v_L =10 THz, v_T =6.9 THz) have overlapping or similar cut-off frequencies than Al-quartz (v_L =4 THz, v_T =1.8 THz), and the cut-off frequencies for Al and sapphire are much higher than Al and quartz. This means phonon flux is higher at the Al/sapphire interface than Al/quartz interface. This enhancement in phonon flux increases the thermal boundary conductance in Al/sapphire.

Fig. 5.7 shows the comparison of G from the experiment (G_{expt}) and model (G_{model}) as a function of Debye temperature for metals on quartz and sapphire. The blue symbols represent quartz substrate and red symbols represent sapphire substrate. The red square symbol represents the G_{model} for

Al/sapphire (428 K), Al/Ni/sapphire (450 K), and Al/Cr/sapphire (630 K). The red circles represent the G_{expt} for Al/sapphire (428 K), Al/Ni/sapphire (450 K), and Al/Cr/sapphire (630 K). The blue square symbol represents the G_{model} for Al/Quartz (428 K), Al/Ni/Quartz (450 K), and Al/Cr/Quartz (630 K). The blue circle symbol represents the G_{expt} for Al/Quartz (428 K), Al/Ni/Quartz (450 K), and Al/Cr/Quartz (630 K). Overall thermal boundary conductance (G_{model}) was calculated using Eq. 42. We use DMM for calculating the phonon interaction between metals and substrate. The DMM model used in this study follows few basic assumptions, considering: (1) realistic phonon dispersion relations to calculate the transmission coefficient and G (2) isotropic phonon dispersion along crystal growth direction (3) all possible anharmonic processes in the transmission (4) contributions from optical phonons in substrate. The model agrees reasonably well with the experiment. Data from the model supports experimental observations, including discrepancies with predictions. For the Al/sapphire and Al/Ni/sapphire system, the G_{model} is slightly higher than the experimental data. It can be because of two reasons: 1) in the model, we considered contribution from all high-frequency optical phonons in sapphire, but only low-frequency optical phonons are most likely to participate in n-phonon processes; 2) impurities at the surface of substrates can reduce the experimental G. For quartz substrate, model agrees well with the experimental data.

To conclude, materials with intermediate Debye temperature enhanced the thermal boundary conductance in materials. However, due to the discrepancies in Prediction 2 and Prediction 3, Debye temperature is not a good parameter to select the proper interlayer to modify the thermal boundary conductance in metal-dielectric systems.

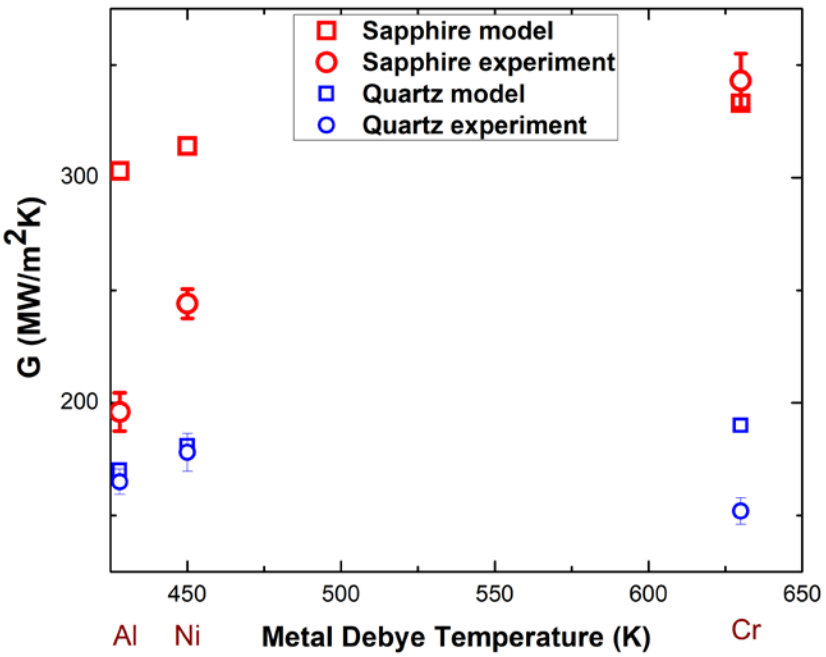

Fig. 5.7. Comparison of G from the experiment (G_{expt}) and model (G_{model}) as a function of Debye temperature for metals on quartz and sapphire. The blue symbols represent quartz substrate and red symbols represent sapphire substrate. The red square symbol represents the G_{model} for Al/sapphire (428 K), Al/Ni/sapphire (450 K), and Al/Cr/sapphire (630 K). The red circles represent the G_{expt} for Al/sapphire (428 K), Al/Ni/sapphire (450 K), and Al/Cr/sapphire (630 K). The blue square symbol represents the G_{model} for Al/Quartz (428 K), Al/Ni/Quartz (450 K), and Al/Cr/Quartz (630 K). The blue circle symbol represents the G_{expt} for Al/Quartz (428 K), Al/Ni/Quartz (450 K), and Al/Cr/Quartz (630 K).

5.3.3 Role of acoustic phonon cut-off frequency

To understand the contribution from acoustic phonon cut-off frequencies, we analyzed the G modification at Au/AlN and Au/sapphire interfaces on insertion of metals with intermediate cut-off frequency. Along with this, we performed a comparative study of substrates with similar Debye temperature but different phonon cut off frequencies. We analyzed two set of samples. First set

had Au/AlN (reference sample), Au/Ni/AlN, and Au/Cr/AlN. The second set had Au/sapphire (reference sample) Au/Ni/sapphire, and Au/Cr/sapphire. The corresponding *G*-value measured from experiments are, 35 $MWm^{-2}K^{-1}$, 88 $MWm^{-2}K^{-1}$, 54 $MWm^{-2}K^{-1}$, 50 $MWm^{-2}K^{-1}$, 260 $MWm^{-2}K^{-1}$, and 225 $MWm^{-2}K^{-1}$,respectively for the above-listed samples. The thermal model mentioned in the above section was used to analyze the experimental data. Fig. 5.8 shows a comparison of experimental and theoretical thermal boundary conductance between Au/AlN, Au/Ni/AlN, Au/Cr/AlN and Au/sapphire, Au/Ni/sapphire, Au/Cr/sapphire. Sapphire and AlN have similar Debye temperatures: 1047K and 1150K, respectively. However, both experiment and model shows that, $G_{Au/sapphire} > G_{Au/AlN}$, $G_{Ni/sapphire} > G_{Ni/AlN,}$ and $G_{Cr/sapphire} > G_{Cr/AlN}$. This observation agrees with the Prediction 6, which states that if two materials have overlapping cut-off frequencies, *G* enhances due to the increase in the phonon flux at the interface. The previous analysis on Debye temperature also suggests that thermal boundary conductance modification can be better predicted using cut-off frequencies rather than Debye temperature. Sapphire (~10 THz) has low-frequency acoustic phonons close to Cr (9.6 THz) and Ni (9.1 THz), whereas for AlN (~18 THz) the phonon cut-off frequencies are higher compared to interlayers. This significantly reduces the overall thermal boundary conductance for AlN samples due to reduced phonon flux at the interface. The experimentally observed trend for the samples on AlN is that $G_{Au/Ni/AlN} > G_{Au/Cr/AlN} > G_{Au/AlN}$, and for the samples on sapphire we observed a similar trend that $G_{Au/Ni/sapphire} > G_{Au/Cr/sapphire} > G_{Au/sapphire}$. However, the experimental trends are not in agreement with the predictions 4 and 5 for the lowest value for Au/AlN and Au/sapphire samples. On the other hand, the model agrees with the Predictions 4 and 5. Comparisons of the Cr/sapphire value with Al as the top metal layer and Cr/sapphire value with Au as the top metal layer shows a significant change in thermal boundary conductance. However, for Ni/sapphire thermal boundary conductance with Al and Au as top

layers remains unchanged. This difference can be attributed to the weak electron-phonon coupling in Au and the subsequent changes in heat transfer pathways on addition of an interlayer with strong coupling constant. This is explained in the following section.

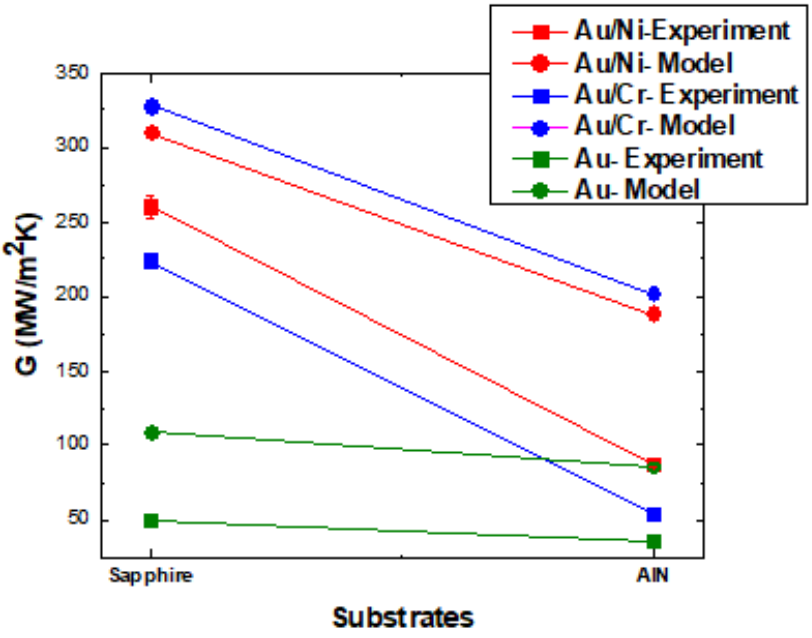

Fig. 5.8. Comparison of experimental and theoretical thermal boundary conductance between Au/AlN, Au/Ni/AlN, Au/Cr/AlN and Au/sapphire, Au/Ni/sapphire, Au/Cr/sapphire. Green square represents the G_{expt} for Au in sapphire and AlN. Green circle represents the G_{model} for Au in sapphire and AlN. Red square represents the G_{expt} for Au/Ni in sapphire and AlN. Red circle represents the G_{model} for Au/Ni in sapphire and AlN. Blue square and circle represents the G_{model} and G_{expt} for Au/Cr in sapphire and AlN respectively.

To summarize, insertion of materials with intermediate acoustic phonon cut-off frequencies can enhance the thermal boundary conductance due to an increase in phonon flux at the interface. Cut-off frequency is a better parameter than Debye temperature to predict the modification of thermal boundary conductance in the presence of an interlayer. However, this is

limited only for systems with top metal having relatively strong *g*. If the metal layer has a weak *g*, then the effects of electron-phonon coupling should be considered.

5.3.4 Role of electron-phonon coupling constant

To understand the effect of strong non-equilibrium in the metal layer, we deposited Au on sapphire and AlN. Au, due to its low electron-phonon coupling strength, is an ideal material for studying the electron-phonon energy transfer mechanisms and its effects on *G* in the presence of an interlayer. The *G* at Au/sapphire interface measured experimentally in the absence of interlayer was ~50 $MWm^{-2}K^{-1}$. This is in agreement with previously reported Au/sapphire *G* values ranging between 50 $MWm^{-2}K^{-1}$ - 70 $MWm^{-2}K^{-1}$ [13], [14], [40]. On addition of interlayers, the measured value for Au/Al/sapphire, Au/Ni/sapphire, and Au/Cr/sapphire are ~95 $MWm^{-2}K^{-1}$, 260 $MWm^{-2}K^{-1}$, and 225 $MWm^{-2}K^{-1}$ respectively. We used the thermal model described in section 5.3.2 to compare with the experimental data as shown in Fig. 5.8. The addition of interlayers with stronger *g* than Au at Au/sapphire enhanced the overall thermal boundary conductance. The enhancement is expected (Prediction 7) and is in accordance with the experiment. However, the magnitude of *G* value, measured for Al (5 nm)/sapphire and Cr (5 nm)/sapphire with Au as a top metal layer, is reduced with respect to the *G*-value measured with Al as a top metal layer on sapphire substrate. Fig. 5.9 also shows that for Al (5 nm)/sapphire and Cr (5 nm)/sapphire the measured *G*-value is completely in disagreement with calculated *G* from model. This clearly shows that the strong non-equilibrium in Au has a profound effect in determining the overall interfacial transport. This can be attributed to the strong electron-phonon coupling in the interlayer, which facilitates the ‘back transfer’ of heat to the metal layer. Heat transfer from interlayer to substrate happens at a time

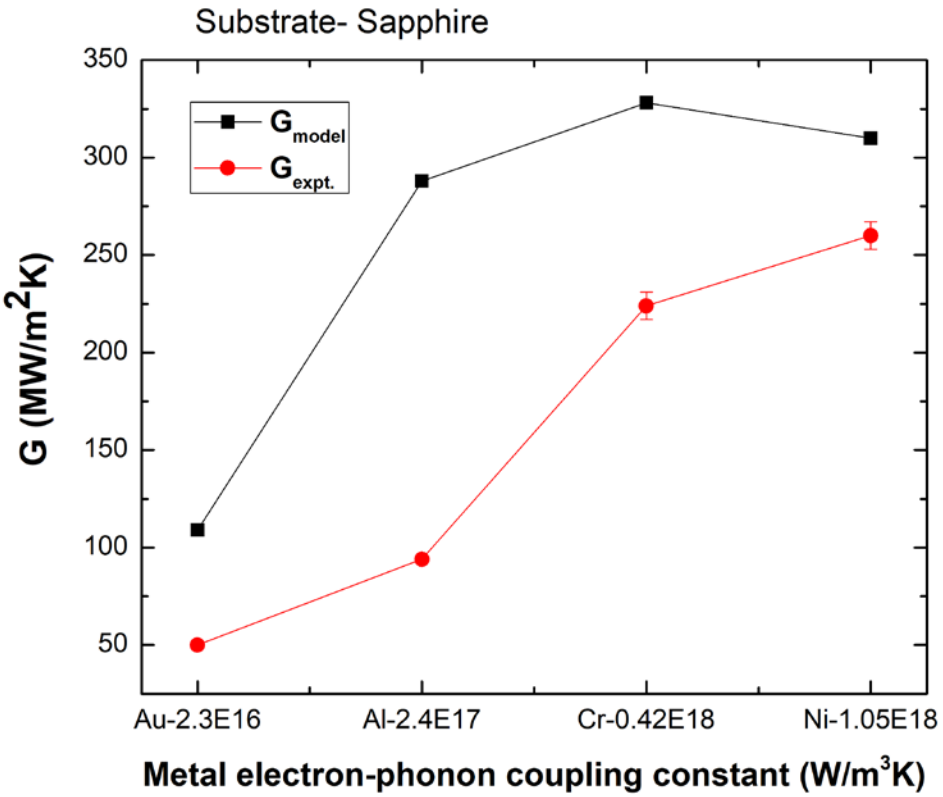

Fig. 5.9. Comparison of G from the experiment ($G_{expt.}$) – red – and model (G_{model}) – black – as a function of metal electron-phonon coupling strength g.

constant much higher (small $G_{pp,2}$) than interlayer to metal. This results in a backpropagation of heat from interlayer back to the metal layer (low resistance pathway comparing to $G_{pp,2}$). Since the thermal model does not account for the backflow of heat, model overestimates the overall conductance in Au/Al/Sapphire and Au/Cr/sapphire systems. In order to analyze the role of various interlayers on heat transfer and back propagation, we calculated the time taken for heat to equilibrate in various metals. Table 5 shows the equilibrium time constant for different metals in this study. The electron-phonon relaxation time is much shorter in Au/Al/sapphire system comparing to other metals; this facilitates the heat backflow to the metal. As the equilibrium time

constant decreases, the energy carriers in the interlayer reaches an equilibrium faster and transfers the remaining heat back to the Au layer.

Further, we analyzed another set of Au samples on AlN substrate. The measured Au/AlN thermal boundary conductance was ~35MWm^{-2}K^{-1}. Inserting a Cr and Ni layer in between Au and AlN enhanced thermal boundary conductance to 55 MWm^{-2}K^{-1} and 90 MWm^{-2}K^{-1}, respectively. Fig. 5.10 shows the comparison of G from the experiment (G_{expt}) and model (G_{model}) as a function of metal electron-phonon coupling strength g in Au/AlN sample set. For the AlN substrates, the model overestimates the actual experimental values. The difference between model and experiment is higher for AlN substrate than sapphire substrate. This is because of two reasons. First, heat transfer from interlayer to AlN happens at a larger time constant than sapphire due to the small G between AlN and interlayer. Hence, heat transferring rate back to the metal increases,. Moreover, the difference between model and experiment is higher for the Au/Cr/AlN system than the Au/Ni/AlN system. As explained before, this difference is due to the higher equilibration time in Cr, which promotes back transfer. Second, accounting for the high-frequency optical branches in AlN model can overestimate the data because, in reality, probability for higher order anharmonic processes decreases with increasing number of phonons (or large energy difference).

Jeong et al. and Weber et al. performed experiments on insertion of Cu interlayer in between Au/sapphire and Au/sapphire, diamond, Si interfaces [13]. They did not observe back transfer in Cu samples despite the weak electron-phonon coupling in Cu. This can be attributed to the longer equilibration time constant in Cu. Table 5 shows that both Cu and Ni have similar and higher equilibration time with respect to other metals. The higher time constant in Ni slows down the back transfer process and, hence, has a negligible effect on overall thermal boundary conductance, as evident from the experiment results.

Table 3: Calculation of equilibrium time constant for different metals

Metal	**g (W/(m^3 ·K))**	**$C_e=\gamma_e T$ (J/m^{3}K)**	**C_p (J/m^{3}K)**	**Time constant (τ)** $\tau_{metal}^{-1} = g\left(C_e^{-1} + C_p^{-1}\right)$
Au	0.023×10^{18}	21450	2.40×10^{6}	1ps
Al	0.24×10^{18}	273608	2.43×10^{6}	112fs
Cr	0.42×10^{18}	58050	3.24×10^{6}	136fs
Ni	1.05×10^{18}	323220	3.96×10^{6}	285fs
Cu	0.10×10^{18}	29430	3.5×10^{6}	294fs

It is apparent that the two conditions for backflow mentioned in section 5.1 are necessary but not sufficient. As observed from the experiments and analysis, the interlayer equilibration time should be short for the backpropagation to happen. Hence, in addition to those conditions, the electron-phonon equilibration time in interlayer also should be considered.

In summary, we found that the transport mechanisms are different in the presence of a top metal layer with strong electron-phonon non-equilibrium such as Au. Addition of an interlayer with stronger electron-phonon coupling strength enhances the overall interfacial conductance by reducing the resistance due to electron-phonon non-equilibrium. However, depending on the time taken by the interlayer to equilibrate electron-phonon population and the time taken for interlayer to heat transfer to the dielectric, an additional pathway can be created. The resistance due to this

additional pathway can significantly reduce the overall thermal boundary conductance. The thermal model, not accounting for the additional resistance channel, overestimates the experimental results.

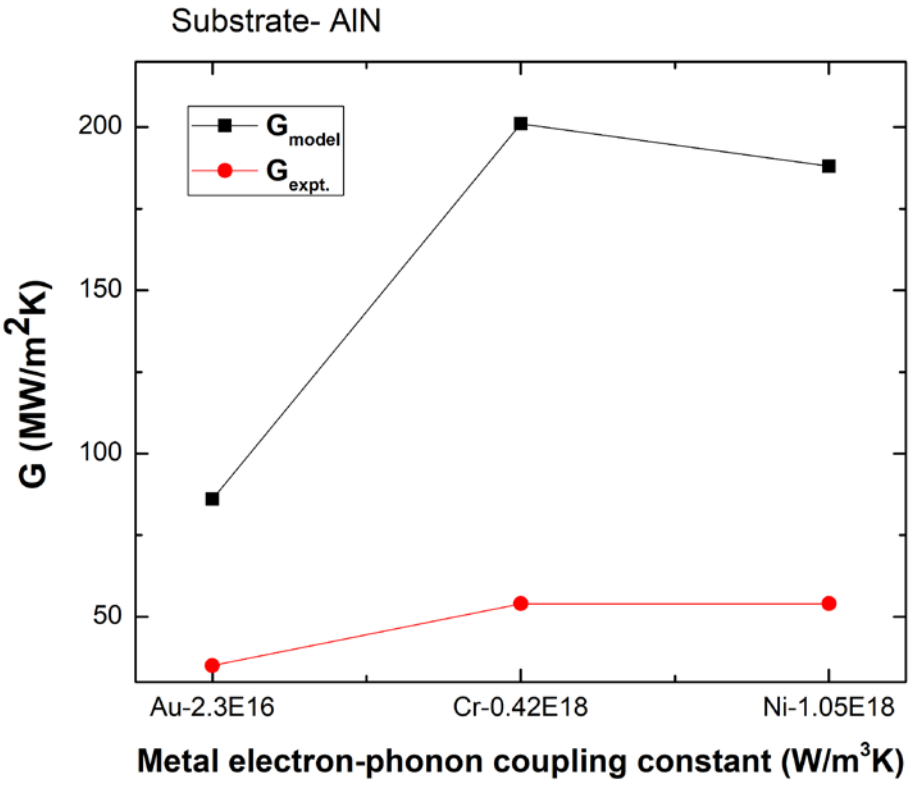

Fig. 5.10. Shows the comparison of G from the experiment ($G_{exp.}$) – red – and model (G_{model}) – black – as a function of metal electron-phonon coupling strength *g* in Au/AlN sample set.

5.4 Conclusion

In this chapter, we analyzed the mechanisms of heat transport on insertion of a 5 nm interlayer at metal-dielectric interface. We propose that the modification of thermal boundary

conductance involves an interplay between phonon spectra overlap and electron-phonon coupling strength of the interlayer. When the non-equilibrium between electrons and phonons in the top layer is strong, inserting a metal layer with strong electron-phonon coupling than the metal layer can facilitate the back transfer of heat to the metal layer, which in turn reduces the overall thermal conductance. When the electron-phonon non-equilibrium in the top layer is weak, the overall thermal boundary conductance is primarily governed by phonon frequency overlap between interlayer and substrate. This phonon frequency overlap can be better explained in terms of cut-off frequency overlap rather than Debye temperature overlap. Hence, cut-off frequency is a good measure to describe the phonon spectra overlap. Thus, this study helps in determining the proper interlayer for systematically enhancing or reducing the thermal boundary conductance at any metal-dielectric interface.

CHAPTER 6

CONCLUSION

This thesis primarily analyzes the modification of thermal transport at a metal-dielectric interface in the presence of an interlayer. Addition of an appropriate interlayer can modify interfacial properties resulting in enhancement or reduction of thermal boundary conductance. Analysis of various thermal transport mechanisms that contribute to thermal boundary conductance is vital in selection of an interlayer. This thesis is mainly dedicated to understanding the thermal transport mechanisms that contribute to the overall thermal boundary conductance in metal-dielectric systems on insertion of metallic interlayers. To summarize, this thesis analyzes the following questions:

1) How does *G* vary with interlayer thickness?

   We found that the addition of an ultrathin interlayer at metal-dielectric interfaces significantly alters the thickness-dependent thermal boundary conductance until it reaches a plateau. The saturation thickness or the evolution of thermal boundary conductance is determined by the volumetric electron-phonon coupling constant (*g*) of the metals. If the top metal layer has a strong coupling constant (e.g. Al), then the *G* evolution trend is solely determined by the electron-phonon coupling constant of the interlayer. On addition of an interlayer with much stronger coupling constant than the top metal layer, the thickness-dependent *G* saturates faster within ~2 nm. If the top metal layer has a weak coupling constant (e.g. Au), then the saturation thickness is determined by the electron-phonon coupling constants for both the top metal and interlayer.

2) Which heat transfer pathways are dominant in the presence of a particular interlayer?

The dominant heat transfer pathways in the presence of an interlayer depend primarily on the volumetric electron-phonon coupling constant for the metal and interlayer. If the top metal layer has a strong enough g, then the resistance due to the electron-phonon non-equilibrium in this layer is negligible, and hence the contribution to the thermal conductance from that pathway can be ignored. On addition of an interlayer with even stronger g at this interface, the heat transfer pathways are controlled by phonon-top metal/phonon-dielectric interaction, electron-top metal/electron-interlayer interaction, electron-interlayer/phonon-interlayer interaction, and phonon-interlayer/phonon-dielectric interaction. If the interlayer thickness is higher than the largest phonon wavelength in top metal layer, then the contribution from phonon-top metal/phonon-dielectric interaction is negligible.

When the top metal layer has a weak g, the resistance due to the electron-phonon non-equilibrium in this layer adds a resistance channel to the above-mentioned interactions. In addition, insertion of an interlayer with stronger g can add another resistance channel depending on the electron-phonon equilibration time in the interlayer. If the equilibration time for electron-phonon interaction in the interlayer is short, the heat can transfer back to the metal, creating additional resistance channel. The three necessary conditions for this channel to be effective are:

i) The g for top metal should be weak and the interlayer should have a higher g than top metal layer.

ii) The equilibration time for electrons and phonons in the interlayer should be short.

iii) The time taken by heat to transfer from interlayer-dielectric should be much higher than time taken to transfer from interlayer-metal.

In short, the strength of volumetric electron-phonon coupling in the interlayer and metal plays a significant role in determining the dominant heat transfer pathway channels in metal-interlayer-dielectric system.

3) What interlayer properties enhance/reduce the *G*?

The two important interlayer properties that determine the modification of *G* at metal-dielectric interfaces are phonon spectra and electron-phonon coupling strength of the metals. Good overlap between phonon spectra of the metal, interlayer, and substrate enhances the overall *G* due to the increase in phonon flux at the interface. On the other hand, electron-phonon coupling strength of the interlayer (along with top metal's *g*) determines the possible heat transfer pathway channels in a metal-interface-dielectric system. The strong coupling strength of the interlayer reduces the non-equilibrium between electrons and phonons, thereby enhancing the overall *G*. The effect of *G* is more pronounced in systems with top metals having weak *g*.

Thus, for metal-interlayer-dielectric systems with top metal having strong electron-phonon coupling constant, the phonon spectra overlap predominantly determines the modification of thermal boundary conductance. Adding an interlayer with intermediate phonon spectra can enhance the *G* due to enhancement in the phonon flux and *G* can be reduced by adding interlayers with mismatching phonon spectra. On the other hand, for metal-interlayer-dielectric systems with top metal having weak electron-phonon coupling constant, the modification of thermal boundary conductance involves an interplay between phonon spectra overlap and coupling strength of interlayer.

4) How to select an interlayer to enhance/reduce *G*?

As mentioned in the previous paragraph, phonon spectra and electron-phonon coupling of the interface are the two important parameters that can significantly modify the thermal boundary conductance. We found that a good parameter to measure the phonon spectra overlap in metal-interlayer-dielectric system is the 'acoustic phonon-cut-off frequency'. Good overlap between acoustic cut-off frequencies of the materials in the above system can enhance *G*.

Selecting an interlayer for enhancing/reducing *G* primarily involves the following procedures:

i) Check the electron-phonon coupling strength of the top metal layer

ii) If the top metal layer has a strong enough *g*, inserting an interlayer with intermediate acoustic cut-off frequency enhances the *G* by bridging phonon transport. To reduce *G*, adding an interlayer with mismatching acoustic phonon frequency works.

iii) If the top metal layer has a weak *g*, inserting an interlayer with intermediate acoustic cut-off frequency enhances the *G* by bridging the phonon transport, but the magnitude of the thermal boundary conductance increment is limited by the resistance due to non-equilibrium in the interlayer.

It should be noted that since our experiments were based on interlayers with strong electron-phonon coupling constant, these procedures assume that the inserted interlayer has a stronger coupling constant than the top metal layer.

BIBLIOGRAPHY

[1] F. Rosei, “Nanostructured surfaces: challenges and frontiers in nanotechnology,” *J. Phys. Condens. Matter*, 2004.

[2] G. Chen, “Nanoscale Energy Transport and Conversion,” *Nanoscale Energy Transp. Convers.*, 2005.

[3] D. G. Cahill *et al.*, “Nanoscale thermal transport,” *Journal of Applied Physics*. 2003.

[4] D. G. Cahill *et al.*, “Nanoscale thermal transport. II. 2003-2012,” *Applied Physics Reviews*. 2014.

[5] A. A. Balandin and D. L. Nika, “Phononics in low-dimensional materials,” *Materials Today*. 2012.

[6] N. Yang *et al.*, “Thermal interface conductance between aluminum and silicon by molecular dynamics simulations,” *J. Comput. Theor. Nanosci.*, 2015.

[7] Z. Tian, S. Lee, and G. Chen, “Heat Transfer in Thermoelectric Materials and Devices,” *J. Heat Transfer*, 2013.

[8] R. Yang, G. Chen, and L. Anand, “Nanoscale Heat Conduction with Applications in Nanoelectronics and Thermoelectrics Supervisor,” *Archives*, 2006.

[9] N. Yang, X. Xu, G. Zhang, and B. Li, “Thermal transport in nanostructures,” *AIP Advances*. 2012.

[10] P. Brinks and M. Huijben, “Thermoelectric oxides,” in *Epitaxial Growth of Complex Metal Oxides*, 2015.

[11] M. S. Dresselhaus *et al.*, “New directions for low-dimensional thermoelectric materials,” *Adv. Mater.*, 2007.

[12] J. A. Bain, J. A. Malen, M. Jeong, and T. Ganapathy, “Nanoscale thermal transport

aspects of heat-assisted magnetic recording devices and materials," *MRS Bull.*, 2018.

[13] M. Jeong *et al.*, "Enhancement of Thermal Conductance at Metal-Dielectric Interfaces Using Subnanometer Metal Adhesion Layers," *Phys. Rev. Appl.*, 2016.

[14] M. Blank and L. Weber, "Influence of the thickness of a nanometric copper interlayer on Au/dielectric thermal boundary conductance," *J. Appl. Phys.*, 2018.

[15] C. Jeong, S. Datta, and M. Lundstrom, "Thermal conductivity of bulk and thin-film silicon: A Landauer approach," *J. Appl. Phys.*, 2012.

[16] K. Charles, *Introduction To Solid State Physics 8Th Edition*. 2003.

[17] A. Jain *et al.*, "Commentary: The materials project: A materials genome approach to accelerating materials innovation," *APL Materials*. 2013.

[18] G. Chen, R. Yang, and X. Chen, "Nanoscale heat transfer and thermal-electric energy conversion," *J. Phys. IV*, 2008.

[19] K. E. Goodson and Y. S. Ju, "HEAT CONDUCTION IN NOVEL ELECTRONIC FILMS," *Annu. Rev. Mater. Sci.*, 2002.

[20] G. Chen, "Phonon heat conduction in nanostructures 1," *Int. J. Therm. Sci.*, 2000.

[21] A. Majumdar and P. Reddy, "Role of electron–phonon coupling in thermal conductance of metal–nonmetal interfaces," *Appl. Phys. Lett.*, 2004.

[22] A. Giri, B. M. Foley, and P. E. Hopkins, "Influence of Hot Electron Scattering and Electron–Phonon Interactions on Thermal Boundary Conductance at Metal/Nonmetal Interfaces," *J. Heat Transfer*, 2014.

[23] J. Lombard, F. Detcheverry, and S. Merabia, "Influence of the electron-phonon interfacial conductance on the thermal transport at metal/dielectric interfaces," *J. Phys. Condens. Matter*, 2015.

[24] S. Sadasivam, U. V. Waghmare, and T. S. Fisher, “Electron-phonon coupling and thermal conductance at a metal-semiconductor interface: First-principles analysis,” *J. Appl. Phys.*, 2015.

[25] A. Giri *et al.*, “Mechanisms of nonequilibrium electron-phonon coupling and thermal conductance at interfaces,” *J. Appl. Phys.*, 2015.

[26] P. E. Hopkins and P. M. Norris, “Substrate influence in electron-phonon coupling measurements in thin Au films,” *Appl. Surf. Sci.*, 2007.

[27] A. Giri and P. E. Hopkins, “Role of interfacial mode coupling of optical phonons on thermal boundary conductance,” *Sci. Rep.*, 2017.

[28] E. T. Swartz and R. O. Pohl, “Thermal boundary resistance,” *Rev. Mod. Phys.*, 1989.

[29] A. Balandin and K. L. Wang, “Effect of phonon confinement on the thermoelectric figure of merit of quantum wells,” *J. Appl. Phys.*, 1998.

[30] J. C. Duda and P. E. Hopkins, “Systematically controlling Kapitza conductance via chemical etching,” *Appl. Phys. Lett.*, 2012.

[31] P. E. Hopkins *et al.*, “Manipulating thermal conductance at metal-graphene contacts via chemical functionalization,” *Nano Lett.*, 2012.

[32] M. Shen, W. J. Evans, D. Cahill, and P. Keblinski, “Bonding and pressure-tunable interfacial thermal conductance,” *Phys. Rev. B - Condens. Matter Mater. Phys.*, 2011.

[33] Y. Wang, Z. Lu, A. K. Roy, and X. Ruan, “Effect of interlayer on interfacial thermal transport and hot electron cooling in metal-dielectric systems: An electron-phonon coupling perspective,” *J. Appl. Phys.*, 2016.

[34] T. S. English, J. C. Duda, J. L. Smoyer, D. A. Jordan, P. M. Norris, and L. V. Zhigilei, “Enhancing and tuning phonon transport at vibrationally mismatched solid-solid

interfaces," *Phys. Rev. B - Condens. Matter Mater. Phys.*, 2012.

[35] Y. P. Chen, Y. Wang, X. Li, X. Ruan, and W. Park, "Reducing interfacial thermal resistance between metal and dielectric materials by a metal interlayer," *J. Appl. Phys.*, 2019.

[36] R. Cheaito *et al.*, "Thermal boundary conductance accumulation and interfacial phonon transmission: Measurements and theory," *Phys. Rev. B - Condens. Matter Mater. Phys.*, 2015.

[37] P. E. Hopkins and P. M. Norris, "Relative Contributions of Inelastic and Elastic Diffuse Phonon Scattering to Thermal Boundary Conductance Across Solid Interfaces," *J. Heat Transfer*, 2009.

[38] J. Zhu, D. Tang, W. Wang, J. Liu, K. W. Holub, and R. Yang, "Ultrafast thermoreflectance techniques for measuring thermal conductivity and interface thermal conductance of thin films," *J. Appl. Phys.*, 2010.

[39] A. J. Schmidt, "Optical Characterization of Thermal Transport from the Nanoscale to the Macroscale," *Ph.D thesis MIT*, 2008.

[40] R. Cheaito, C. S. Gorham, A. Misra, K. Hattar, and P. E. Hopkins, "Thermal conductivity measurements via time-domain thermoreflectance for the characterization of radiation induced damage," *J. Mater. Res.*, 2015.

[41] Y. K. Koh *et al.*, "Comparison of the 3ω method and time-domain thermoreflectance for measurements of the cross-plane thermal conductivity of epitaxial semiconductors," *J. Appl. Phys.*, 2009.

[42] Y. Wang, J. Y. Park, Y. K. Koh, and D. G. Cahill, "Thermoreflectance of metal transducers for time-domain thermoreflectance," *J. Appl. Phys.*, 2010.

[43] C. A. Paddock and G. L. Eesley, “Transient thermoreflectance from thin metal films,” *J. Appl. Phys.*, 1986.

[44] J. P. Feser, J. Liu, and D. G. Cahill, “Pump-probe measurements of the thermal conductivity tensor for materials lacking in-plane symmetry,” *Rev. Sci. Instrum.*, 2014.

[45] J. P. Feser and D. G. Cahill, “Probing anisotropic heat transport using time-domain thermoreflectance with offset laser spots,” in *Review of Scientific Instruments*, 2012.

[46] P. Jiang, X. Qian, and R. Yang, “Time-domain thermoreflectance (TDTR) measurements of anisotropic thermal conductivity using a variable spot size approach,” *Rev. Sci. Instrum.*, 2017.

[47] A. J. Schmidt, X. Chen, and G. Chen, “Pulse accumulation, radial heat conduction, and anisotropic thermal conductivity in pump-probe transient thermoreflectance,” *Rev. Sci. Instrum.*, 2008.

[48] D. G. Cahill, “Analysis of heat flow in layered structures for time-domain thermoreflectance,” *Rev. Sci. Instrum.*, 2004.

[49] A. Feldman, “Algorithm for solutions of the thermal diffusion equation in a stratified medium with a modulated heating source,” *High Temp. - High Press.*, 1999.

[50] M. Kazan, “Interpolation Between the Acoustic Mismatch Model and the Diffuse Mismatch Model for the Interface Thermal Conductance: Application to InN/GaN Superlattice,” *J. Heat Transfer*, 2011.

[51] P. Reddy, K. Castelino, and A. Majumdar, “Diffuse mismatch model of thermal boundary conductance using exact phonon dispersion,” *Appl. Phys. Lett.*, 2005.

[52] J. C. Duda, T. E. Beechem, J. L. Smoyer, P. M. Norris, and P. E. Hopkins, “Role of dispersion on phononic thermal boundary conductance,” *J. Appl. Phys.*, 2010.

[53] P. E. Hopkins, “Multiple phonon processes contributing to inelastic scattering during thermal boundary conductance at solid interfaces,” *J. Appl. Phys.*, 2009.

[54] P. E. Hopkins, J. C. Duda, and P. M. Norris, “Anharmonic Phonon Interactions at Interfaces and Contributions to Thermal Boundary Conductance,” *J. Heat Transfer*, 2011.

[55] P. E. Hopkins, P. M. Norris, and R. J. Stevens, “Influence of Inelastic Scattering at Metal-Dielectric Interfaces,” *J. Heat Transfer*, 2008.

[56] J. C. Duda, J. L. Smoyer, P. M. Norris, and P. E. Hopkins, “Extension of the diffuse mismatch model for thermal boundary conductance between isotropic and anisotropic materials,” *Appl. Phys. Lett.*, 2009.

[57] T. Beechem, J. C. Duda, P. E. Hopkins, and P. M. Norris, “Contribution of optical phonons to thermal boundary conductance,” *Appl. Phys. Lett.*, 2010.

[58] J. C. Duda *et al.*, “On the assumption of detailed balance in prediction of diffusive transmission probability during interfacial transport,” *Nanoscale Microscale Thermophys. Eng.*, 2010.

[59] P. E. Hopkins *et al.*, “Influence of anisotropy on thermal boundary conductance at solid interfaces,” *Phys. Rev. B - Condens. Matter Mater. Phys.*, 2011.

[60] B. C. Gundrum, D. G. Cahill, and R. S. Averback, “Thermal conductance of metal-metal interfaces,” *Phys. Rev. B - Condens. Matter Mater. Phys.*, 2005.

[61] V. Shalagatskyi, “Ultrafast acoustics in hybrid and magnetic structures,” 2015.

[62] O. Kovalenko *et al.*, “Generation of ultrashort acoustic pulses in cobalt by ballistic electrons in gold,” 2013.

[63] W. Wang and D. G. Cahill, “Limits to thermal transport in nanoscale metal bilayers due to weak electron-phonon coupling in Au and Cu,” *Phys. Rev. Lett.*, 2012.

[64] R. J. Stevens, A. N. Smith, and P. M. Norris, “Measurement of Thermal Boundary Conductance of a Series of Metal-Dielectric Interfaces by the Transient Thermoreflectance Technique,” *J. Heat Transfer*, 2005.

[65] S. Gnanarajan, S. K. H. Lam, and A. Bendavid, “Coexistence of epitaxial Ta(111) and Ta(110) oriented magnetron sputtered thin film on c-cut sapphire,” *J. Vac. Sci. Technol. A Vacuum, Surfaces, Film.*, 2010.